Experimental Fluid-Structure Interaction

On Providing Reliable Experimental Data for Validation of Fluid Structure Interaction in ComFlow

Babafemiwa Olajide

Technische Universiteit Delft

TU Delft Delft University of Technology

Challenge the future

EXPERIMENTAL FLUID-STRUCTURE INTERACTION

ON PROVIDING RELIABLE EXPERIMENTAL DATA FOR VALIDATION OF FLUID STRUCTURE INTERACTION IN COMFLOW

by

Babafemiwa Olajide
S.N.: 4506863

in partial fulfillment of the requirements for the degree of

Master of Science
in Offshore and Dredging Engineering

at the Delft University of Technology,
to be defended publicly on Tuesday August 29, 2017 at 11:00 AM.

Supervisor:	Dr. ir. P. R. Wellens	
Thesis committee:	Prof. dr. ir. A. P. R. van 't Veer,	TU Delft
	Dr. ir. P. R. Wellens,	TU Delft
	Ir. P. de Vos,	TU Delft

An electronic version of this thesis is available at http://repository.tudelft.nl/.

TU Delft Delft University of Technology

"If you want to find the secrets of the universe, think in terms of energy, frequency and vibration."

– Nikola Tesla

Acknowledgements

Performing this thesis project would have not been possible without the help and support of several people. As such, I would like to thank them for helping me throughout the process.

My sincerest gratitude first goes to my supervisor – Peter Wellens, for entrusting me with this research exercise and believing in my abilities to carry it out excellently. For always giving me the extra push at seeming roadblocks and your critical approach toward my thesis – being there to guide me all through the thesis process.

Very crucial to the success of this research, also, was Peter Poot; thanks for providing all the practical support I needed and especially for making my ideas a physical reality. Many thanks to Hans van der Hek, for assisting with the many fabrication jobs needed in building my experimental setup.

Last but not the least, I would like to thank my friends and family. Thanks to my parents for the encouraging words which really had a stimulating effect on me. Thanks to Briggs, Sahil, Fredo, Joost for sharing the struggle and helping me out. Those long days at 3mE with lots of Dutch coffee breaks eventually paid off.

Babafemiwa Olajide

Delft, August 2017

Abstract

Structures at sea, which can either be floating or bottom-founded, are always affected by several types of dynamic loads from wind, waves and currents; with floating offshore structures subjected to more motion and loading from these loads. Hence, necessitating more in-depth hydrodynamic analyses. Increasing size and weight of the floating structures together with industry demands have led to unsuitability of existing models – which make use of rigid body (no hydroelasticity) assumptions. This, in addition to other reservations about current practices, has led to the need for more realistic formulations of the interaction between fluids and our offshore structures, taking hydroelasticity into account. Extreme wave impacts, which are responsible for severe damage of offshore structures, have for a long period been only studied with experimental methods, as the non-linear nature of the complex wave kinematics make solutions not straightforward. More recent advancements have seen the development of numerical techniques and programs, based on the Navier-Stokes equations, to better understand extreme waves and impacts on offshore structures.

This thesis focuses on the topic of experimental validation of *fluid-structure interaction* in ComMotion – an advancement in the ComFLOW program (an improved Volume of Fluid (iVOF) Computational Fluid Dynamics (CFD) code) to capture motion of flexible structures in the presence of free surface effects and a two-way coupling between the fluid and the structure. This has led to the need to provide reliable data for validation purposes. The research is conducted in continuation of the studies carried out by Rizos [1] in which an electromagnetic drive linear motor produced *noise* and variable amplitude enforcement obtained in the analyzed results, amidst other uncertainties in the measurement techniques used. The current methodology principally makes use of a different motion technique – rotary to linear motion.

Firstly, rotary to linear motion was chosen (motivated from the internal combustion engine of an automobile) and then verified computationally with analytical derivations. The experiments were then designed, with the initial step being to verify the said linear motion. A sensitivity of the motion signal to weights in the system was carried out. Further, the experiment designed made use of a latex rubber membrane, applied with a clamped boundary condition at the bottom of a partially-filled rigid cylindrical structure. Tension existing in the membrane, due to water columns above it, was analytically obtained, as complete knowledge of system parameters was crucial. Linear oscillatory motion at the end of the converted rotary motion was applied to the fluid-structure system. Motion signals were obtained – rigid body measurements, to subtract them from the membrane motion measurements obtained. Motion measurements were acquired with laser triangulation displacement devices and a force transducer was used to monitor applied forces in the plunger during the experiments. The output of the transducer can offer validation data to the FSI solver.

Membrane measurements were taken at half radius at a 30° step over a 180° span, and at the centre. This was in a bid to capture maximum deflections of the membrane, as interest was to capture the *coupled frequency* mode shape. Finally, the obtained membrane motion data were analysed to prove their reliability, and to draw conclusions from them. Volume (*of*

liquid), frequency and polar dependence analyses were carried out. Recommendations were subsequently outlined, for future research.

CONTENTS

List of Figures

List of Tables

NOMENCLATURES

T	Membrane tension
w	Membrane deflection as a function of spatial coordinate x
P	Pressure due to water column acting on membrane
L	Span of membrane in tension analysis
w_{max}	Maximum deflection at membrane centre due to water column
h_0	Initial water height assuming rigid plunger bottom
ρ	Density of water
g	Acceleration due to gravity
h^*	New water height after membrane is deflected
k	Wave number in membrane analysis
A_i	Amplitudes of sine-fit components
f_i	Frequencies of sine-fit components
ϕ	Phase difference between sine-fit components

List of Abbreviations

CFD	**C**omputatoional **F**luid **D**ynamics
DAQ	**Data Aq**uisition
DOF	**D**egree **o**f **F**reedom
FPSO	**F**loating **P**roduction **S**torage and **O**ffloading
FRF	**F**requency **R**esponse **F**unction
FSI	**F**luid **S**tructure **I**nteraction
iVOF	**i**mproved **V**olume **O**f **F**luid
LDV	**L**aser **D**oppler **V**ibromter
MAC	**M**odal **A**ssurance **C**riterion
PSV	**P**olytec **S**canning **V**ibrometer
PTFE	**P**oly**T**era**F**luoro**E**thylene
PVC	**P**oly**V**inyl**C**hloride
RBM	**R**igid **B**ody **M**otion
SSE	**S**um of **S**quares due to **E**rror
VIV	**V**ortex **I**nduced **V**ibration

1

INTRODUCTION

1.1. GENERAL INTRODUCTION

Fluid – Structure Interaction (FSI), in the broad sense of it, is generally what happens when the motions of a fluid and solid are somehow coupled. Coupling at the fluid-solid interface is usually described by kinematic (velocities) and dynamic (forces) conditions. This interaction can be noticed in events in everyday life; such as around us – when leaves flutter in wind, inside us – when our hearts beat, above us – when the wings of an air plane vibrates, and as interesting to this study, on the sea, when our offshore structures are stationary or in motion. Domains of application of FSI are Civil engineering, Aerospace engineering, Food processing, Nuclear engineering, Ocean engineering, Marine/Offshore engineering and Biomechanics, to mention a few. The importance of the study of FSI cannot be overemphasized, as it helps us to understand and mitigate an extensive range of problems such as flutter, galloping, sloshing, Vortex-Induced Vibration (VIV), amongst others.

1.1.1. FLUID-STRUCTURE INTERACTION OFFSHORE

Structures at sea, which could either be floating or bottom-founded, are always affected by several types of dynamic loads, with environmental effects such as waves, wind and currents being the most important sources of motions and structural responses in a seaway [4]. Floating offshore structures on the other hand such as offshore oil production systems, conventional ships and mono- or multi- hull vessels, are subjected to more motion, warranting the need for more in-depth hydrodynamic analyses. The increasing size and weight of floating offshore structures, coupled with industry demands for more slender and faster vessels, has led to the unsuitability of existing models that make assumptions of rigid bodies (no hydroelasticity is considered). This increase in dimension results in a decrease of the overall stiffness, resulting in natural frequencies so low, that they are near the exciting frequencies. More so, the approach of rigid body modelling leads to more several structural response due to overestimation of the water pressure [5]. A more realistic formulation of the interaction between the fluids and our offshore structures is hence necessary. One theory that provides an alternative is the hydroelastic theory.

1.1.2. HYDROELASTICITY

Hydroelasticity can be referred to as the branch of Fluid-Structure Interaction (FSI) that is concerned with the motion of deformable bodies through water. There exists a coupling between the motions (both rigid body and structural vibrations) of the structure and the hydrodynamic forces. Hydroelastic design practices try to incorporate the influence of dynamic properties of offshore structures in this coupling for better prediction of responses. It is only fair then to say that engineering analyses for seaway-induced dynamic responses prediction of offshore systems should be based on a realistic formulation of the FSI domain via integration of structural mechanics, hydrodynamics and use of new and unconventional modelling methods [4].

With the interest in- and need for- developing better FSI tools, good emphasis must be placed on the variability of the physical processes that occur in the different areas of application. Relevant to the offshore engineering field of application is the inclusion of the free-surface. This introduces a coupling process between a two-phase fluid flow and the structure of interest. Numerically, there exists broad variety of methods applicable, with each leading to varying accuracies and efficiencies [6]. The need to assess the applied methods arise; and validation data obtained from well-controlled fundamental experiments can indeed be very useful in validating the investigated processes.

1.2. PROBLEM STATEMENT

Incidents like the damage suffered to the bow of the Schiehallion Floating Production Storage and Offloading (FPSO) vessel by wave impact on the night of November 9, 1998 [7] have spurred research in the direction of better understanding of the interaction between the environment and offshore structures, both stationary and moving. Extreme wave impacts, which are responsible for this kind of damage, have for a long period been only studied with experimental methods, as the non-linear nature of the complex wave kinematics do not make it straightforward. More recent advancements have seen the development of numerical techniques or programs, based on the Navier-Stokes equations, to better understand extreme waves and impacts on offshore structures.

To develop guidance, calculation methods and risk assessment procedures for green water and wave impact loading, SAFE-Flow project was initiated. An advancement from the SAFE-Flow project was ComFLOW, which is an Improved Volume of Fluid (IVOF) Computational Fluid Dynamics (CFD) code to compute non-linear wave loads on offshore structures [8]. ComFLOW-2 implemented the generation of waves by specifying fluid velocities, obtained from potential flow, at the inflow boundary of the fluid domain. ComFLOW-3 focused on the development and validation of complex free surface turbulent flows in the offshore industry with improved functionality and speed-up of the algorithms [9]. With all these as precursor, the need to improve the computational tool to cover moving and deforming objects in extreme waves arose. Hence, the ComFLOW-4 (ComMotion) project was initiated – focusing on the development of a highly-complex novel unsteady two-way numerical coupling technique, and possessing a mathematical approach comprising of a unified numerical coupling of the fluid-body interaction and the hydroelastic deformation. This would lead to new insights in design procedures for ships in waves; as used by ship-building companies.

This research focuses on the topic of experimental validation of FSI in ComMotion. An advancement in the ComFLOW program to capture motion of flexible structures, in the presence of free surface effects and a two-way coupling between the fluid and the structure, has

led to the need to provide reliable data for validation purposes. The research is conducted in continuation of the studies carried out by Rizos [1], which was a reduced-complexity experiment to obtain data for validation of FSI in a CFD program. Use was made of an electromagnetic drive linear motor, which was attributed to the noise obtained in the analyzed results, amidst other uncertainties in the measurement technique of using a Digital Image Correlation (DIC) system. Due to the low reliability of the resulting data, the need for designing a modified procedure and obtaining more reliable data is necessary.

1.3. RESEARCH OBJECTIVE

The development of a coupling algorithm robust enough to handle the two- or multi- way coupling of fluid and structure domains, in the non-linear multi-physics nature of FSI problems is not quite a walk in the park. And due to lack of analytical models, there is a need of experimental data for validation. To obtain the validation data, several considerations would have to be made. Of major importance, would be incorporating the underlying physics needed to be reproduced in the target computational tool i.e. ComMotion. This would include free surface effects and coupling between the fluid (water) and the structure. Furthermore, the reproducibility of the experiment in ComMotion at no extra computational cost is necessary. This would mean that the experiment has a simple geometry, with possible symmetries, as complicated geometries for both fluid and structure domains necessitate finer unstructured grids for accurate solution at the boundary layer regions and therefore, need to be avoided. One important aspect would be to ascertain the level of accuracy of the validation data. The results should also be processed, to ensure that the measurements are reliable enough to be used as validation data for an FSI computational tool. Of minor importance, would be semblance of the physical experiment to any problem encountered in real – life (such as slamming). Sloshing would also need to be avoided when choosing and/or executing the parameters of the experimental matrix.

1.4. BACKGROUND

Over the last decades, extensive research (both theoretical and experimental has been conducted in the interest of understanding the free vibration characteristics of fluid-plate coupled interactions. A lot of these prior research arose from the use of liquid propellants in rockets and missile-flight systems; as the motion of the liquid fuel, if coupled sufficiently with that of the structure, would produce large responses. Undoubtedly, the response of a plate or membrane in contact with a fluid is different from its response in air. It is agreed that the eigen frequencies when coupled with a liquid is always less than those in air. Relating to the experimental setup of this research, numerous prior investigations have been conducted on cylindrical containers filled with liquids due to the wide applicability, and can be found in literature.

Bhuta [10, 11] studied the coupled oscillations of a liquid with a free surface in a cylindrical tank with a membrane bottom for small motions of the liquid surface, for both axisymmetric and symmetric cases; and concluded that the effect of the membrane bottom on the axisymmetric sloshing frequencies is small for most engineering problems. The same problem was investigated by [12]. [13] investigated the coupled oscillation of liquid in an annular circular cylindrical container with a flexible bottom, in which the first two mode shapes of the free surface of the liquid and the corresponding mode shapes of the annular membrane of the bottom were determined. [14] examined the nonlinear longitudinal oscillation of liq-

uid in a circular cylindrical container with an elastic bottom. [15, 16] also investigated the hydroelastic vibrations of liquid in varied configurations – in a rectangular container and a circular cylindrical container, respectively, in which the liquid free surface was covered by an elastic plate or flexible membrane. [17, 18] studied the axisymmetric free vibration of the flexural bottom plate in a liquid-filled cylindrical container supported on an elastic foundation under the consideration of the effect of in-plane force in the plate due to the static liquid pressure. [19] and [20] studied the modes where the walls oscillate, moving the liquid, of an elastic bottom in circular and annular cylindrical containers partially filled with liquid by using the Ritz method.

The present study takes similarity with the general case of the clamped elastic bottom in a rigid cylindrical container (hereafter referred to as plunger), but has some fundamental differences. The plunger would contain a liquid, and altogether immersed in a larger-size liquid concentric cylindrical container. The plunger will be oscillated, by applying an external vertical sinusoidal force, effectively applying a vertical periodic motion to the boundaries of the membrane. Hydroelastic vibrations of the circular membrane at the bottom of the plunger, in the liquid, would then be measured.

2

METHODOLOGY

2.1. OBJECTIVES OF THE EXPERIMENTS

Defining the goals of experiments prior to carrying them out, is very important in experimental research thesis. The aims of the experiments are outlined below.

1. To simulate a coupled fluid – structure system. This means that the fluid flow around the structure should influence the structure's motion, which in turn should influence the fluid flow field.

2. To offer validation data for any FSI numerical solver. This objective greatly influences the chosen experimental setup, as reproducing the experiment in the solver is key. Hence, contrary to desired field of application of the study, the experiment does not have any direct semblance to typical marine/offshore scenarios.

3. To offer validation data to the FSI solver currently developed by TU Delft i.e. ComMotion. Hence, the experiment is expected to capture physical processes that the solver is intended to cover, namely

    - Fluid-Structure Interaction
    - Free-surface effects
    - Hydroelasticity

4. To also offer data, that can be used to validate numerical and analytical solutions also being developed for fluid-structure interaction problems.

2.2. APPROACH: BASE EXCITATION OF MEMBRANE

To establish the validation data for an FSI computation tool, an experiment with a flexible plate, at the bottom of a plunger (hollow cylinder), fully submerged in a bigger cylinder, is the proposed final setup. The plunger is to be commensurately filled with water, to balance out the hydrostatic pressure from the submergence of the membrane. This filling is aided by two holes drilled on the sides of the plunger, to allow for varying water heights as the plunger is oscillated. The system is setup in such a way that the excitation is imposed directly to the membrane, and not through a disturbance via the fluid field. This would increase

the chances of obtaining significant deflections to be measured, and alleviating the need to correlate the natural frequencies of the membrane with the oscillation frequency. Although, oscillating at the natural frequencies of the membrane would be desirable. To obtain the desired final setup, a series of important sub-experiments must be conducted. These are as outlined below.

2.3. FIRST EXPERIMENT: TO VERIFY THE OSCILLATORY MOTION

This experimental step would be the most important and critical step in achieving the goal of reliable data. To verify the oscillation, the drive system would be set up. This drive system would use an electric rotational motor as the prime mover – producing rotary motion, which would be converted into translational motion via a system of reduction gears, belt, rod and bearings. An intermediate step in verifying the oscillatory motion would be to test the bearings and linkages. This is to ensure that motions in undesirable directions (*e.g.* lateral) are not present. After the motion system is setup and the bearings and linkages are satisfactorily checked, the plunger is fixed at the end of the translational motion. A triangulation laser displacement sensor is placed above the plunger, pointing downward toward the top flange of the plunger, and would measure the motion of the rigid body. Triangulation sensors do not work optimally when the laser beams are passed through transparent media [21]. Hence, the triangulation device would be placed above the plunger, with its beam aimed at the upper part of the plunger which would not be submerged.The motion is started, and the laser displacement sensor measures the motion of the plunger. The signal obtained from the sensor would be processed and evaluated, and compared with the already known computational signal results (see Appendix A). This way, any deviation of the sensor's processed signal from the actual ideal computational signal is noticed, and thus would indicate the unreliability or errors of the motion system. The goal however, is to obtain motion signals that perfectly correspond to the computational signal.

2.3.1. MEASURING INSTRUMENTS/SETUP

Based on the experiment's aim, the setup to achieve this is discussed and a description of the components that would make up the setup is outlined.

1. **Triangulation Laser Displacement Measurer**

   Purpose

   The laser triangulation sensor in this experiment measures only the motion imposed to the plunger.

   Measuring Principle

   The laser displacement measuring device works on a principle of triangulation, which in essence, determines the location of a point, which the laser emits upon, by similar triangles. The sensor emits a laser beam to the object whose position or displacement is to be measured. Position sensitive detectors at the back of an optic lens (positioned perpendicular to the incident ray) receive split laser beams reflected from the measured object. From this, as seen in Figure 2.1, the position of the object is determined by the

distance between the pixels on which the split laser beams impact, using the principle of similar triangles

$$\text{Position} = AB \tag{2.1}$$

$$= AC * \frac{EC}{ED} \tag{2.2}$$

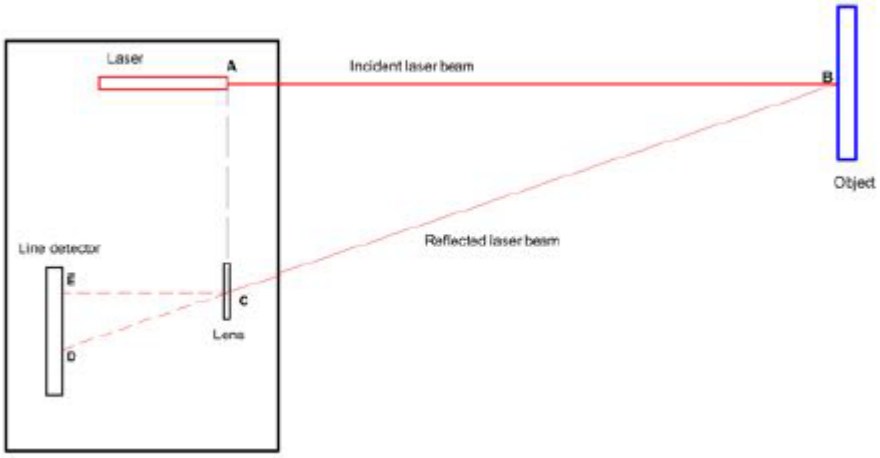

Figure 2.1: Optical triangulation operating principle (source: Rizos 2016)

The size of pixel array on the position sensitive detectors influences the measuring range of the sensor. For triangulation sensors, there is an upper limit and also a lower limit for the measurable distance [21]. Triangulation sensors can have accuracies of up to several micrometers, but it must be noted that this accuracy can reduce with increasing measurement distances.

Technical Characteristics
The triangulation sensor used for the current experiments, is manufactured by *Micro-Epsilon Messtechnik* and borrowed from the measurement shop of *Mechanical, Maritime and Materials Engineering* faculty of TU Delft. The technical specifications of the sensor used, are shown in Table 2.1.

2. Rotary Motor and Frequency Control Drive

Purpose
This serves the purpose of being the prime mover, for this initial experiment and further ones. The motor is a 3-Phase squirrel cage motor, manufactured by *ABB Motors* and is a single-speed motor. Hence, the need to couple it with a frequency drive to vary the speed. The motor would be used together with a *T-Verter* adjustable frequency AC motor drive controller. This incorporates a high-efficiency Pulse Width Modulated

ILD 1401 – 200 Specifications	
Laser type	Semiconductor laser
Laser class	Class 2
Laser wavelength	670 nm
Measuring range	100 mm
Minimum stand-off distance	60 mm
Resolution (static)	20 μm
Resolution (dynamic)	100 μm
Measuring rate	1 kHz
Spot diameter	2100 μm
Voltage output (analogue)	1 .. 5 V
Current output	4 .. 20 mA
Dimensions	65 × 50 × 20 mm

Table 2.1: Laser triangulation displacement measurer Micro-Epsilon ILD 1401 – 200 technical data

(PWM) design and advanced Insulated-Gate Bipolar Transistor (IGBT) technology. The output of which allows a variable speed control of the motor.

Technical Characteristics

The rotary DC motor used for generating the rotational motion before it is converted to linear motion, is manufactured by *ABB Motors* and obtained from the Ship Hydromechanics and Structures' *Towing Tank* of TU Delft. The technical specifications of the motor are shown in Table 2.2.

ABB Motor Specifications	
Bearing	6202 – 2ZC3
Insulation class	ICLF
Laser wavelength	670 nm
Frequency	50 Hz
Voltage	380 – 420 V
Speed	2800 r/min
Power	0.25 kW
Power factor	0.69
Torque	0.84 N·m
Two speed motor	No

Table 2.2: Rotary motor 3GAA061312-ASC technical data

3. Stepped rotary to linear motion mechanism

Based on the high speed of the motor, in comparison with oscillation frequencies of interest for the set of experiments, there is need to reduce the motor speed considerably. For this purpose, a set of toothed gear reduction, with a belt would be employed. The wheels employed would have a reduction ratio of 6 : 1, which is from 10 teeth on the driving gear and 60 teeth on the driven. This can be depicted in Figure 2.2 below. This

set of toothed speed reduction system, when coupled with the adjustable frequency drive controller described earlier, would enable the desired oscillation frequencies to be achieved. It is also important to state that based on the reduction ratio of the rotational speed of the motor, the load (due to the plunger weight, water in and around the plunger and membrane) felt by the motor would be reduced by a factor of six. This would favour the operation of the motor, as it would feel less load, and thus, produce smoother rotational motion.

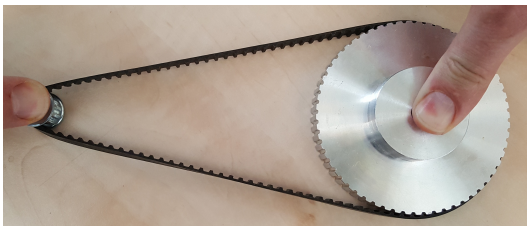

Figure 2.2: 6:1 Toothed belt reduction

4. **Bearings, connecting rod and couplings**

To ensure that the imposed motions are exactly as intended, it is necessary to adopt and place bearings and linkages in positions to help convert the rotational motion to linear sinusoidal motion properly. More so, to prevent the likelihood of undesired motions, bearings are used to ensure that there is no motion in the horizontal plane. These horizontal plane motions could result from standing waves, arising from harmonic motion of the plunger at relatively high frequencies, in later experiments. A schematic of the assembled setup, converting rotational motion to linear sinusoidal motion is as shown in Figure 2.3 below.

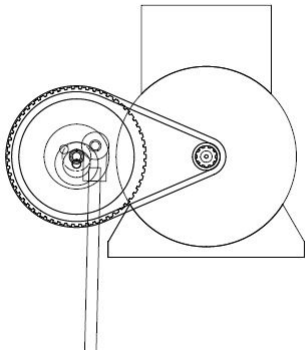

Figure 2.3: Schematic of coupled rotary motor with the reduction toothed wheels

2.4. SECOND EXPERIMENT: TO OBTAIN MEMBRANE VIBRATIONS, WITH PARTIALLY-FILLED PLUNGER

Once the sinusoidal harmonic motion is verified and satisfactory, the next step would be to oscillate the plunger with the membrane at the bottom, with known volumes of water in the plunger. This is done in continuation of the first experiment. In this experiment, the vibrations of the bottom membrane would be measured using a laser triangulation displacement

device; similar to that used in the first experiment. Preference of this measurement equipment over the single point Laser Doppler Vibrometer (LDV) arises from the relatively longer time needed for calibration and setting up of the LDV. More so, the triangulation displacement measurer offers an already quite high scanning frequency (see Table 2.1), which is sufficient to acquire the vibration data. In addition to that, the measurement units are similar (i.e. *metre*) and this avoids the need to first integrate the data obtained (in the case of the LDV), before combination with the rigid body motion signal, to post-process. The motion is then initiated, and the vibrations of the membrane measured. Results of this experiment can be compared to literature, as many studies have been carried out on this. One of these studies is that carried out by Bauer [22], in which the coupled hydroelastic frequencies of a system made up of a circular cylindrical tank with an elastic bottom and filled with a viscous liquid was investigated.

2.4.1. MEASURING INSTRUMENTS/SETUP

In addition to the setup and instruments used in the first experiment, detailed below are additional equipment needed to achieve the second experiment.

1. **Triangulation Laser Displacement Measurer**

Purpose

As the motion of the vibrating membrane at the bottom of the plunger would be the sum of the imposed rigid body oscillatory motions of the plunger and the vibrations of the membrane, one sensor would thus be used to obtain the rigid body motion (RBM), and then subtracted from the vibration of the membrane. The triangulation displacement device used here to measure the membrane vibrations is similar (Table 2.1) to that used in the first experiment (Section 2.3), but only with a higher measuring range of 200 mm and measuring rate of 2 kHz. The sensor would be mounted at the bottom of the plunger, on an *X*-*Y* (Cross) slider, as described in Section 3.1.3. It would be used to measure the motions of the membrane during oscillation.

2. **Force Transducer**

Purpose

This will be installed via a bolted connection just directly above the plunger. It will be used for monitoring the applied force from the linear oscillator mechanism to the plunger. The output of the load cell is very important as it can offer validation data to the FSI solver, by recording the forces experienced by the plunger during the experiment. These forces can be numerically computed in the computational tool by integration of the pressures acting on the wetted surface of the plunger; and thus, compared to the output of the transducer.

Measuring Principle

The force transducer used is a strain gauge load cell of the foil type, with output of an electrical signal. The transducer converts both tensile and compressive forces into

electrical signals by measuring the change in electrical resistance resulting from deformation (strain) when forces (loads) are applied to the sensor.

The change in resistance is measured by a Wheatstone bridge arrangement - which consists of two legs of a bridge circuit, connected with a galvanometer (see Figure 2.4); one of which has an unknown resistance component. There is a calibrated variable resistor in one leg, while the other leg carries the unknown resistor - which is to be measured.

The variable resistor is adjusted so the galvanometer can read zero; and only then would the value of the unknown resistor be computed. After the value is known and the bridge is balanced, the ratios between the resistance values of the same leg are equal:

$$\frac{R_x}{R_A} = \frac{R_{var}}{R_B} \tag{2.3}$$
$$\implies R_x = R_A \cdot \frac{R_{var}}{R_B}$$

The relation between the ratio of the strain-initiated change of resistance ΔR_x to the reference resistance R_x and the strain ϵ is linear:

$$\frac{\Delta R}{R} = GF \cdot \epsilon \tag{2.4}$$

where GF = guage factor representing the sensitivity of the sensor.

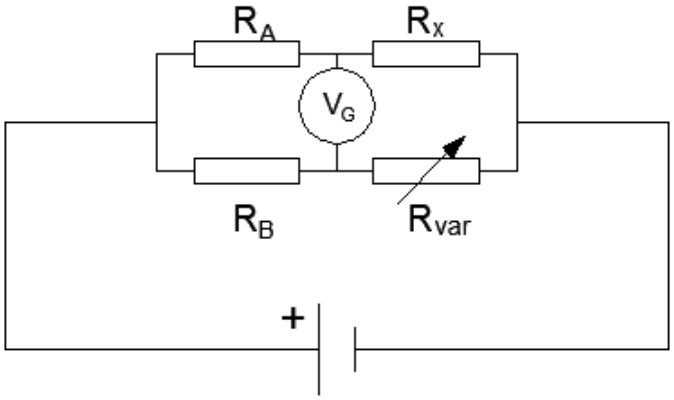

Figure 2.4: Schematic of Wheatstone bridge (source: Rizos 2016)

In Figure 2.4, the resistor R_x represents the strain gauge. Strain gauge load cells have a wide range of rated capacities, and can be used with high resolution digital indicators as force transfer standards. Force transducers can have varying number of gauges, depending on the application - could be temperature compensation or elimination of other strain components or for large strain applications.

Technical Characteristics

A cue for the range of forces experienced by the plunger during measurements was taken from the report by Rizos. The range of force will be related to the oscillation characteristics (frequency and amplitude). The load cell should be able to measure tension

and compression loads, and these should not exceed ±100 N. The specifications of the force sensor are as shown in Table 2.3.

Load Cell Specifications	
Measuring range	±250 N
Ultimate overload	150 %
Safe overload	300 %
Recommended torque on fixation	25 Nm
Principal dimensions	50.8 × 76.2 × 14.5 mm
Material	Nickel-plated alloy steel

Table 2.3: Load cell technical data

3. **Plunger**

The plunger is a hollow cylindrical shape with the membrane at the bottom. The plunger has a shell made of steel with circular slots at its lower tip. These slot are however closed to prevent liquid inside the plunger from spilling out. A hollow hollow PVC cylinder sits inside the shell, and is aligned with the shell by a hole drilled at the top of the shell, just beneath the flange. The membrane is clamped between the lower tip of the PVC cylinder and the steel shell (see Section 3.1.5). The plunger is connected to the oscillation motion-end via a hollow square aluminum beam - attached to the annular lid of the plunger via bolted connections (see Figure 2.5). As per dimensions, the outer diameter of the plunger is 104 mm and its overall height is 157 mm. The circular slot's diameter, that corresponds to the diameter of the bottom's flexible part, is 80 mm.

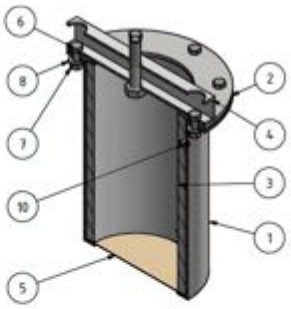

PARTS LIST			
ITEM	QTY	PART NUMBER	DESCRIPTION
1	1	FSI_03	Steel Plunger Shell
2	1	FSI_04	Steel Annular Lid
3	1	FSI_05	PVC Hollow Cylinder
4	1	FSI_06	Aluminium Conection Beam
5	1	FSI_07	PTFE Sheet
6	8	ANSI B18.2.3.1M - M5 x 0,8 x 16	Metric Hex Cap Screw
7	8	ANSI B 18.2.4.1 M - M5 x 0,8	Hex Nut
8	8	ANSI B18.22M - 5 N	Metric Plain Washers
9	1	ANSI B18.2.3.5M - M8 x 1,25 x 40	Hex Bolt
10	1	ANSI B18.3.6M - M4x0,7 x 6	Broached Hexagon Socket Set Screw - Cone Point

Figure 2.5: 3D sectioned view of plunger assembly with list of parts (source: Rizos 2016)

4. **Support Structure**

The aforementioned components for both experiments are mounted on a support structure, with dimensions determined from previous experimental usage - but modified for

current experiments. The support structure comprises of aluminum sections, which are built into vertical and horizontal members and with some as bracings. The structure consists of two parts - the main part and a superstructure. The latter supports the rotary motor, gear reduction and oscillation system and the plunger. A view of the support structure is in Figure 2.6 below.

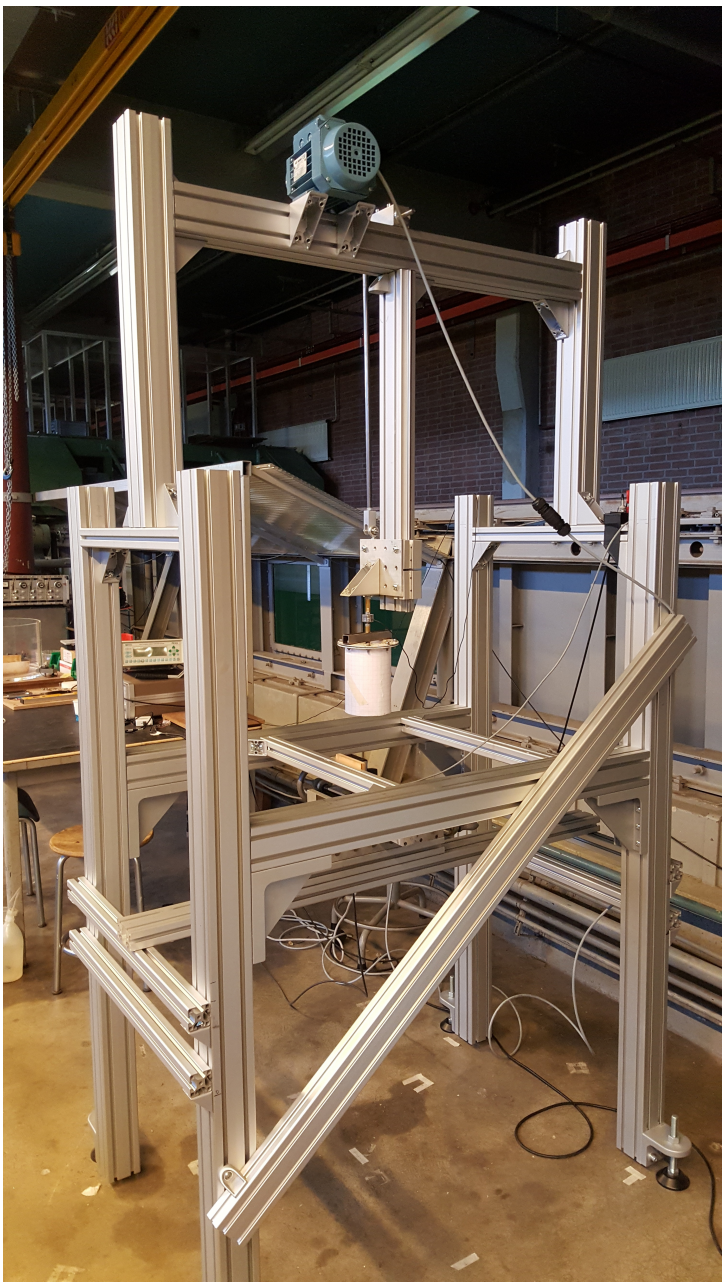

Figure 2.6: View of the support structure as installed

2.5. EXPERIMENTAL MATRIX/PARAMETERS

With all the different experimental procedures defined as above, it is pertinent to determine the experimental matrix. The experiments would consist of motion verification tests and afterwards, forced vibration tests for a membrane (thicknesses 0.2 mm). For the motion verification tests, oscillation frequencies are selected arbitrarily – 1, 2 and 4 Hz are chosen. Interestingly, additional weights are put in the system; – 1 kg and 2 kg to simulate the final experimental scenario which would have more component(s) (partially-filled plunger), resulting in more load in the system. For the amplitudes of oscillation, the three fixed values of 5, 10 and 15 mm are checked.

As per the water volumes in the plunger for the second experiment, values are selected ranging from 50 ml to 400 ml and these have a commensurate height of liquid in the plunger. Low values of water volume are selected to prevent excessing sloshing resulting in water coming out of the plunger, which would compromise the experiments. These water heights would influence the behaviour of the membrane during oscillation. Considering the oscillations, frequencies between 3 Hz and 6.5 Hz are chosen, and these values are obtained from analytical methods from another on-going research. This research takes as input the volume of fluid, membrane density and thickness, and tension in the membrane due to water column above it (See Appendix A). The amplitude chosen is 10 mm; as a higher amplitude would result in excessive water motion in the cylinder – leading to water exiting the plunger, and a smaller amplitude for the chosen frequencies would result in little or no motion in the water to create significant vibrations in the membrane. An overview of the test cases is as shown in Figure 2.7 below.

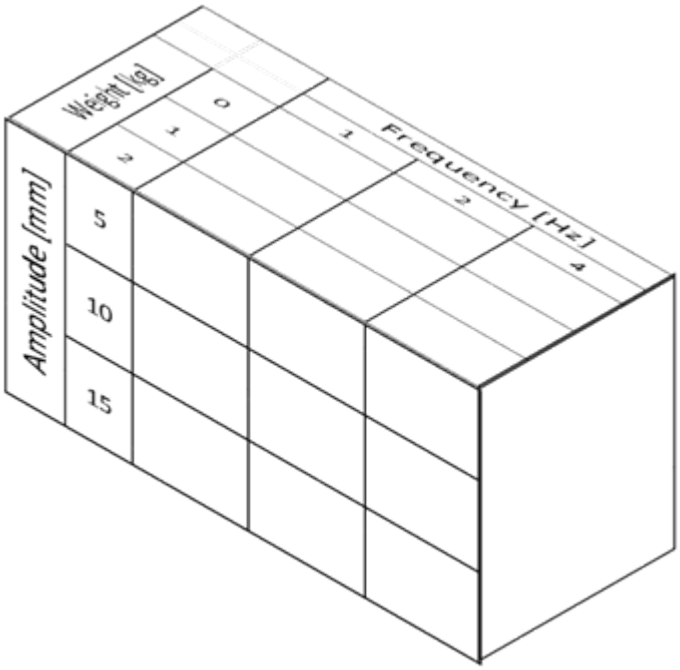

Figure 2.7: Motion verification experiment test matrix

2.5.1. HORIZONTAL POSITIONING OF SECOND SENSOR

During the second experiment, for obtaining the membrane deflections during oscillation, a second sensor (triangulation displacement type) will be used. This has to be positioned horizontally, with consideration given to anticipated location of expected **mode shapes** – in order to avoid nodal points. With the investigated frequencies of oscillation low enough for the fundamental mode of response to dominate, the position of nodal circles are expected at the edges and/or at a co-centric circle of half size. On the contrary, the exact position of nodal diameters cannot be predicted, apart from a single point of them – the centre. With the oscillation frequencies expected to excite the fundamental modes, the laser spot from the triangulation measurement device was decided to be placed at half radius, with measurements taken across a 180° sweep, with a step of 30°. A schematic of the locations is as shown in Figure 2.8 below.

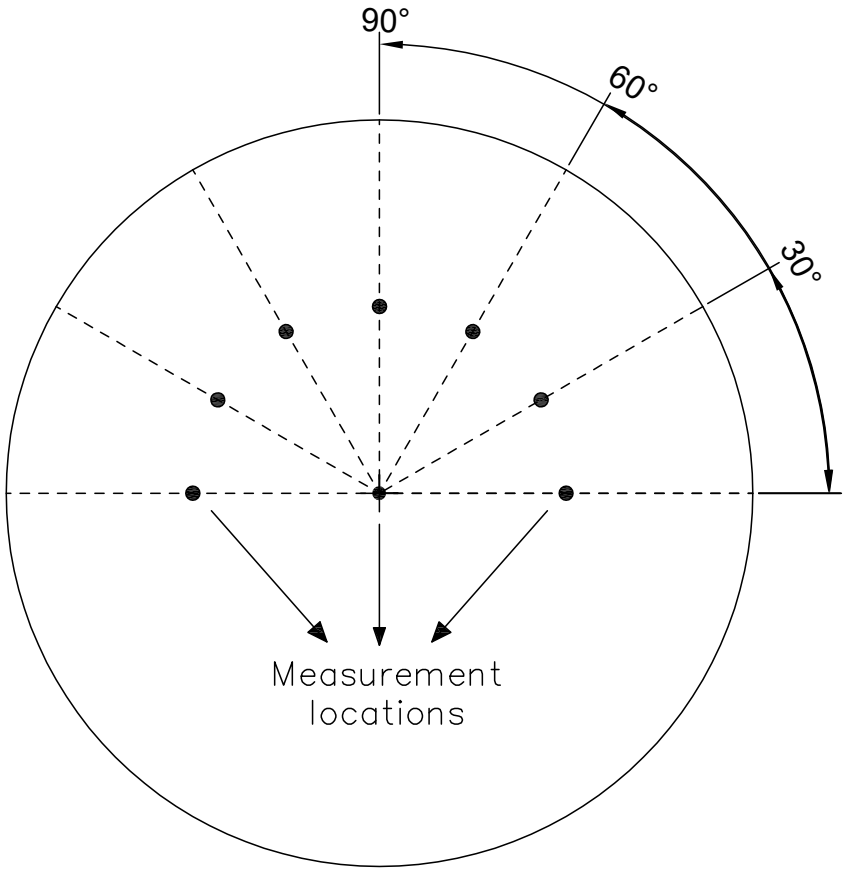

Figure 2.8: Intended measurement locations for second experiment [Plan View]

3

EXPERIMENTAL SETUP - DETAILED DESIGN

3.1. DESIGN CONSIDERATIONS

In order to achieve as accurate results as possible from the intended experiments, the need to ensure that every aspect of the setup functions properly is expedient. To ensure this, the following paragraphs include a detailed description of the aspects considered and suited for the experimental setup.

3.1.1. BEARINGS

To effectively convert the rotational motion, produced by the rotary motor, into linear motion, a good bearing system is needed. Two different bearing systems were created - utilizing spherical sliding bearings and ball bearings respectively; with the latter created due to the limitations of the former. The major difference between them being in the degree of freedom of allowed motion. The following paragraphs describe the approaches due to both bearings.

Spherical sliding bearings

Initially, a spherical sliding bearing is used at both ends of a steel circular rod, connecting the effective rotational motion point to a transition point, which should possess only translational motion (see Figure 3.1). During testing of the system with the bearings, some additional masses are placed at the bottom of the system, and it was noticed that some flexural bending exists in the connecting rod. To cater for this bending, the stiffness of the connecting rod needs to be increased.

According to equation 3.1 below, one possibility of increasing the stiffness of a rod is by increasing the cross-sectional area.

$$k = \frac{EA}{l} \tag{3.1}$$

where k = rod stiffness

E = Young's modulus

A = cross-sectional area

l = length of rod

(a) on the setup

(b) close-up view

Figure 3.1: Spherical sliding bearings at both ends of connecting rod

In line with this, the steel connecting rod, having an initial diameter of $8mm$ is fitted with a hollow steel tube, with an outer diameter of $12mm$. This effectively increases the cross-sectional area of the rod by a factor of 2.25, and thus results in a 125% increase in the stiffness of the rod.

With the issue of bending in the connecting rod solved, further testings are carried out, and a noticeable rotation was present, in addition to some vertical jerky motion. This rotation can be attributed to the inherent design of the spherical sliding bearing, as seen in 3.1b, and as such, necessitates the use of a different type of bearing, to prevent this unwanted motion.

Ball bearings

Ball bearings, known for their strict single degree of freedom - rotational motion, are investigated as a replacement for the spherical sliding bearings illustrated in the previous paragraph. Two cageless ball bearings are mounted on either end of a rectangular rod (see Figure 3.2). The rectangular rod is then mounted in the setup, in place of the initial circular rod with spherical sliding bearings. However better the ball bearings may seem to be, it is worthwhile to note that the design of the bearings make them non - self-aligning, and thus can support only axial loads. Any non-axial loads on the bearing, which could result from even slight misalignments in the system, can possibly damage the bearings.

3.1.2. VERTICAL MOTION

One of the key attributes that the principle of motion generation for the experimental procedures - Crank-slider mechanism hinges on, is enforcement of a perfectly linear motion at the needed end. The linear motion, which is a vertical motion in this case, needs to be enforced as much as possible. The following paragraphs detail the method used to achieve this vertical motion.

(a) on one end

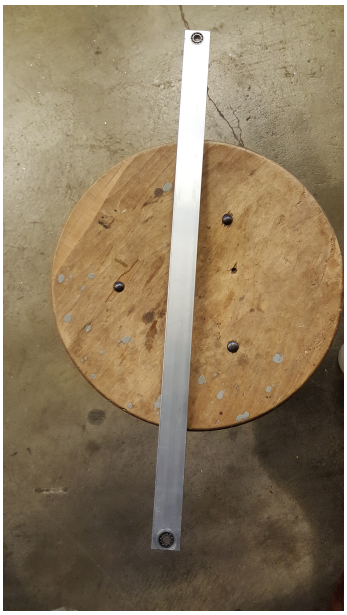

(b) on both ends

Figure 3.2: Cageless ball bearings at ends of rectangular connecting rod

Guiding block

The guiding block is a steel block with dimensions 100 mm ×40 mm ×40 mm, having a square cross-section. A 10 mm diameter hole passes through the block longitudinally, which is lined with a plastic sleeve lubricated with silicon spray for frictionless sliding (Figure 3.3). A slot is made on one side of the block, through which a tightly-fitting circular item is screwed onto the rod passing through the plastic sleeve. This serves to prevent any rotation in the rod, during motion, as this would be undesirable.
This guiding block system, however, does not completely prevent rotational motion, during motion enforcement of the lunger with water in it. Because of this, a different method - rail system - is investigated, to ensure perfect vertical motion during oscillation.

Rail System

The nature of the support structure build-up of the experiment, provides a vertical member right behind the connecting rod. See Figure 2.6. This vertical member, having grooves on either side, is utilized to build up a rail system, as in Figure 3.4. Two steel cylindrical rods, serving as the rails, are inserted into V-shaped slots which fit into the slots on either side of the vertical member of the support structure. Four small sections, with roller wheels inside, are fitted onto the rails, with two on either side. The wheels glide over the rails during motion. The sections have holes onto which a plate is attached, which has an extra member for mounting the plunger onto. This type of connection, with connections on either side of a rod, ensures there is no rotation, given that the rod does not rotate during operation.

3.1.3. $X-Y$ (CROSS-) SLIDER SYSTEM

Since the method of approach of obtaining the deflections of the membrane during imposed oscillation of the plunger involves the use of a *single-point* measurement device, and with

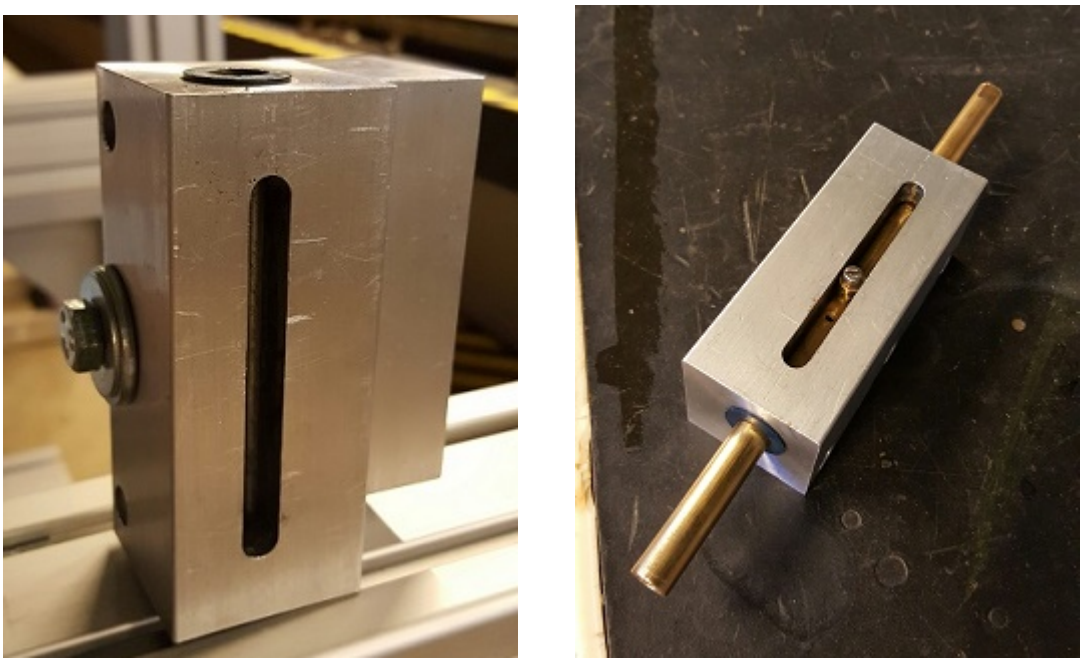

Figure 3.3: Guiding block, as used, showing slot with plastic sleeve

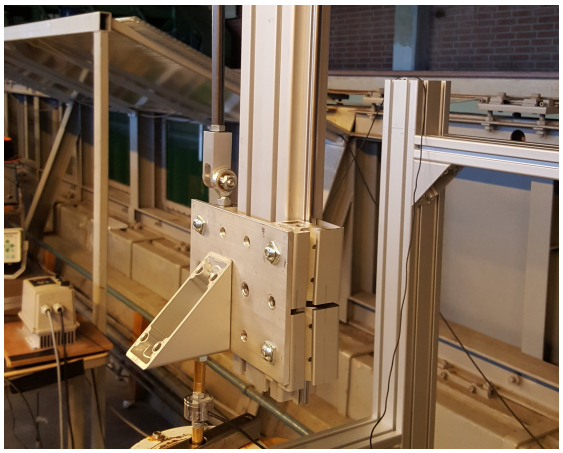

Figure 3.4: Rail system, on vertical beam with grooves, as part of motion system setup

no knowledge beforehand, of which part of the membrane would exhibit the maximum deflections, it is thus necessary to measure various points of the membrane therein. To achieve this, an X-Y (or Cross-) slider system was developed, which would help vary the position of the laser triangulation displacement measurer being used to obtain membrane deflections. See Figure 3.5 below. The cross-slider system consists of two perpendicularly aligned individual sliders, each having mm gradations. Mounting the sliders on each other required a square plate between them, due to the varying hole sizes at the bottom of one slider and the connection point at the top of the sliders.

The sliders need to be aligned properly, to ensure that displacements in say, the Y - slider, occur at exactly 90° to the X - slider.

Perpendicularity

To ensure proper perpendicular alignment of the sliders on each other, they are first mounted on a section, which is fastened to a horizontal member of the support structure. Then, the principle of Pythagorean theorem (In a triangle where one angle is 90° (right angle), the square of the side opposite the right angle is equal to the sum of the square of the other two sides) is employed (equation 3.2), to check the squareness of the connection of the two sliders.

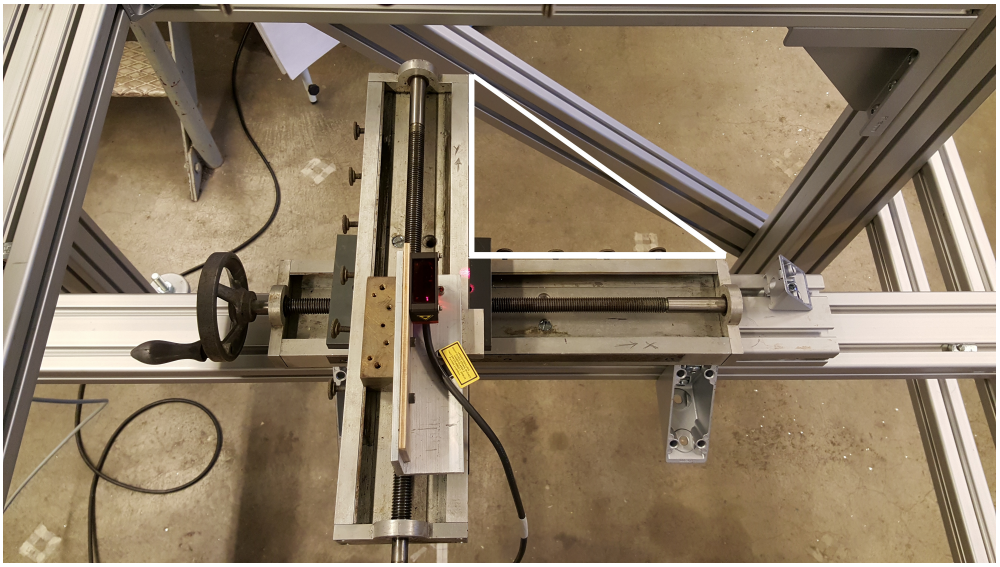

Figure 3.5: Cross-slider, as installed on the experimental setup

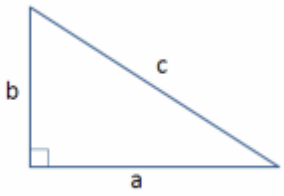

$$c^2 = a^2 + b^2 \tag{3.2}$$

A right-triangle is extracted as shown in Figure 3.5, and the sides measured. The lengths corresponding to a, b and c are measured as:

$$a = 141.5mm$$
$$b = 147mm$$
$$c = 204mm$$

Applying equation 3.2 with the measured a and b values should give a theoretical hypotenuse value of

$$c = 204.04mm$$

This results in an error of 0.02%, in the perpendicularity enforcement.

3.1.4. MATERIAL SELECTION

As the aim of this experimental procedure is to obtain validation data for Fluid-Structure Interaction, the structure used in the experiment should have a significant level of deflection during interaction with the fluid, whilst maintaining its structural integrity. For this to be achieved, some material properties have to be discussed.

Flexibility

The response of the structure is affected by its inherent flexibility and the imposed oscillation. Previous study done by Rizos [1] utilized a PTFE material, considered to be a plate; but due to the low flexibility of the PTFE, a latex material is considered for this experiment (Table.3.1). This choice is better, as it guarantees responses of significant amplitudes during motion and interaction with the fluid. Also, another way to ensure considerable responses is to apply oscillations of frequencies that are in the neighbourhood of the natural frequencies of the coupled fluid and membrane system.

	PTFE	**Latex rubber**
Density [kg/m^3]	2150 - 2200	910 - 930
Young's Modulus [MPa]	410 - 750	1 - 5
Tensile Strength [MPa]	25 - 36	20 - 30
Elongation [%]	350 - 550	750 - 850
Poisson Ratio	0.46	

Table 3.1: Mechanical properties of considered materials (source: Idemat 2003, available at http://www.matbase.com)

3.1.5. BOUNDARY CONDITION ENFORCEMENT

A crucial aspect in the modeling of the structure is the boundary condition. For reasons of convenience, one of the typical boundary conditions (free, simply supported or clamped) should be uniformly applied at the edges. Since simply-supported boundaries on a membrane are difficult to be implemented in physical experiments, it is easier to obtain fully clamped edges successfully. Fully clamped boundary conditions are utilised for the experiments (Figure 3.6). This is achieved by applying uniformly distributed loads (clamps on this case) at the membrane edges. The bolted connections of the plunger (8 M5 bolts) will apply uniformly distributed load to the PVC cylinder and then to the membrane's edges. In this way the fully clamped boundary condition will be obtained.

3.1.6. MEMBRANE TENSION

It is sought to determine the tension existing in a membrane, due to a specified height (or volume) of water, in order to estimate the wet resonant frequencies of the coupled system due to harmonic excitation. Firstly, the physics of membranes must be understood. Membranes can be of two types - *thick* and *thin*, depending on the ratio of their maximum deflection to their thickness. When a membrane's maximum deflection is much larger than its thickness, the membrane is thin and when its maximum deflection is much smaller than its thickness, it is called thick. The membrane of interest in this case is a latex membrane with a thickness

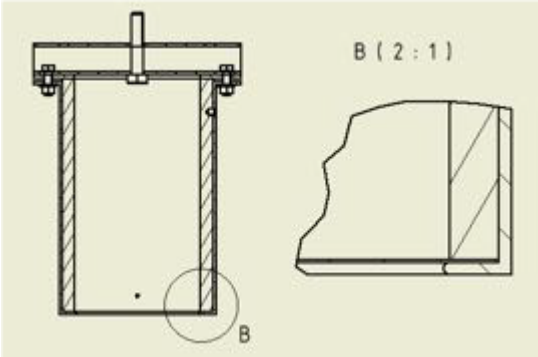

Figure 3.6: Clamped boundary of the membrane, enlarged. (Source: Rizos 2016 [1])

of 0.20 mm; and this, when combined with significant deflections in the order of centimeters, makes it "thin".

With the understanding of the membrane physics, the tension is calculated by solving the differential equation below, presented in detail in Appendix B, for a 2D case.

$$T\,\nabla^2 w + P = 0$$

and

$$P = \rho g(h^* + w)$$

with boundary conditions

$$w(0) = 0$$
$$w(L) = 0$$

where P = pressure due to the water height, acting on the membrane,
T = tension in the membrane, which is to be solved for,
w = membrane deflection, which is a function of the spatial coordinate x, and
h^* = new water height after the membrane has been deflected.

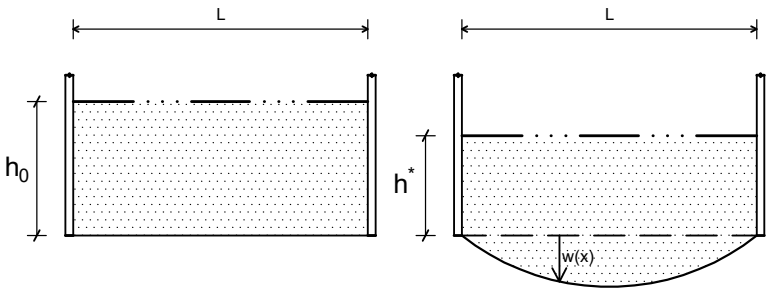

Figure 3.7: Membrane tension schematic – before and after deflection

The solution of equation 3.1.6 yields

$$w = \frac{\rho g h^*}{kT} + \frac{\rho g h^*}{kT}\cos(kx) + \left(\frac{1-\cos(kL)}{\sin(kL)}\right)\sin(kx)$$

which together with the conservation of mass, assuming constant density

$$\int_0^L w(x)\mathrm{d}x + h^* L = h_0 L$$

yields two equations with four unknowns (h^*, T, w and x).

In order to solve the simultaneous equations, the number of unknowns has to be reduced to the number of equations. Hence, *static* experiments are conducted to obtain the maximum deflection of the membrane ($w = w_{max}$) at the centre of the plunger; which occurs at position $x = L/2$ in equation 3.1.6, due to different water columns (figure 3.8). This reduces the unknowns to two (h^* and T), which can then be solved for, thus yielding the membrane tension.

In the experiment to obtain the maximum membrane deflection at the centre, the *major key* was to obtain the centre of the membrane which is located at the bottom fo the plunger. A disc – with a small nudge at the centre – whose diameter equals the inner diameter of the plunger (80 mm) was 3D printed. See Figure 3.9. With the disc inserted in the plunger, the laser ray of the triangulation displacement measurer (sitting on the cross-slider pointing upward) is aimed at the nudge. The methodology, thus, involved obtaining a reference measurement with the membrane fixed at the bottom of the plunger. Then, known volumes of water are put into the plunger, in increasing order, with the centre of the membrane measured again at each volume step. A correlation is then made between the measurements before- and after- water is put, from which their difference gives w_{max}

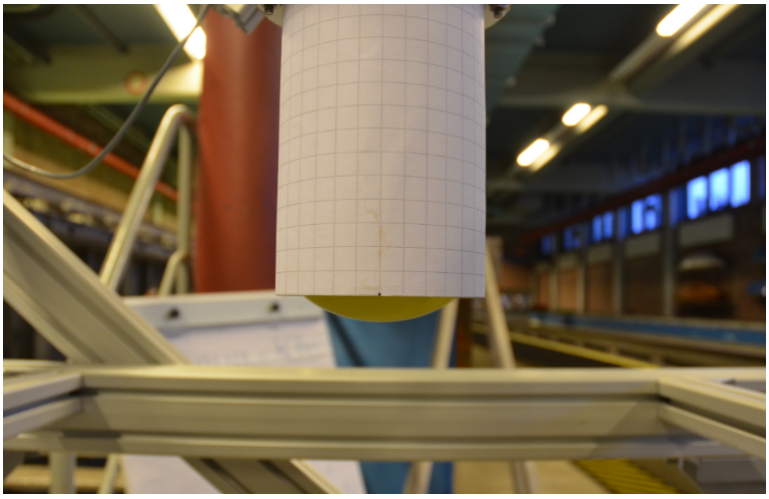

Figure 3.8: Static experiment to obtain w_{max}

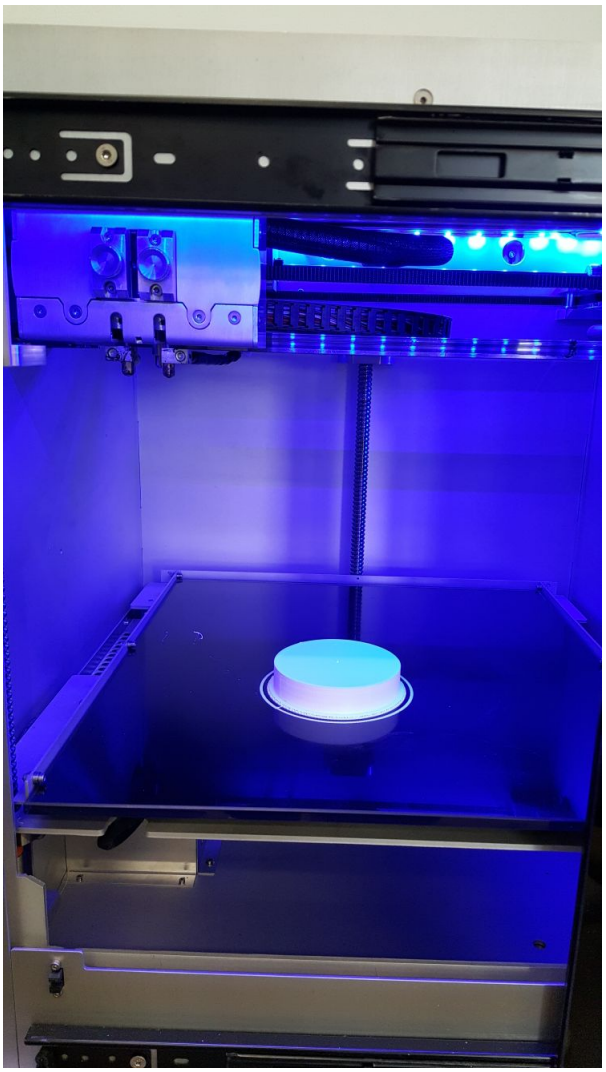

Figure 3.9: 3D printed disc with nudge

4

EXECUTION OF EXPERIMENTS - RESULTS

4.1. INTRODUCTION

The motion data is analysed and presented first, with tables showing the experimental parameters investigated. After this, membrane vibration results are analysed further, with the experimental matrix modified. Reasons for this modification are discussed, and representative cases from the measurement instruments are selected, analysed and presented.

4.2. FIRST EXPERIMENT - MOTION ANALYSIS

For the motion definition of the experiments, different motion signals are obtained per experimental case, as defined in the experimental matrix. However, no case is treated with water; as the motion experiment is conducted by coupling only the top flange of the plunger. In addition to this, to simulate the extra load in the system in subsequent experiments, standard weights are added to the flange and the experiments are run, also per case as defined in the experimental matrix.

4.2.1. CASES INVESTIGATED

Cases investigated are as shown in Table 4.1 below. A few representative cases are chosen,

Case Nr.	Oscillation Amplitude [mm]	Oscillation Frequencies [Hz]	Added Weights [kg]
1	5	1, 2, 4	0, 1, 2
2	10	1, 2, 4	0, 1, 2
3	15	1, 2, 4	0, 1, 2

Table 4.1: Investigated cases - Motion analysis

whose results are analyzed below. One in which no extra weight is added to the system, and another in which a comparison is made between different extra weight sizes added to the system.

1. **Case 1: Amplitude** 15 **mm, Frequency** 2 **Hz, Added weight** 0 **kg**

   With an amplitude of 15 mm and frequency of 2 Hz set as input parameters for the motion. The signal obtained from the triangulation displacement measurer is analyzed in

the frequency domain, and Figure 4.1 below shows the result. It can be seen from the plot that there exists a unique maximum peak, corresponding to the frequency of oscillation. However, the amplitude of this peak is less than the amplitude of oscillation. Also noteworthy is a second peak at double the maximum-peak frequency. This second peak has an amplitude, which is about 2.3% of the maximum amplitude. This is however different from the ratio between the amplitudes obtained from the kinematic analysis in Appendix A.

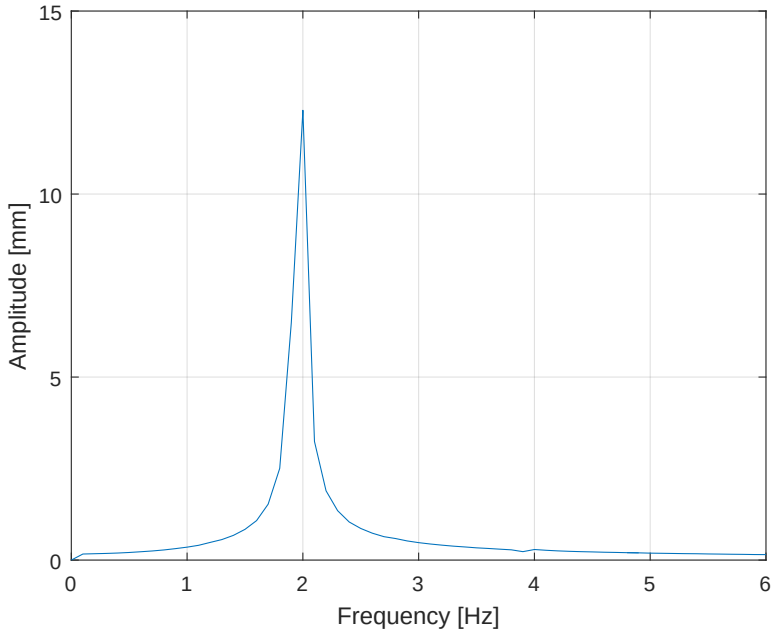

Figure 4.1: Single-sided amplitude spectrum of displacement - Case 1

Furthermore, Table 4.2 below gives a summary of the frequencies and amplitudes obtained by analyzing the time-signal by fitting it with a sine-fit (sum of three sine signals; Equation 4.1), as established in Appendix A. Detailed error analyses is treated in the Chapter 5.

$$f(x) = \sum_{i=1}^{3} A_i * \sin(2\pi f_i x + \phi) \tag{4.1}$$

A15mm, 2Hz, 0kg	Geometric		Experimental	
i =	f [Hz]	A [mm]	f [Hz]	A [mm]
1	2.00	15.00	1.97	13.76
2	0.07	0.12	1.96	1.308
3	3.99	0.1122	2.1	0.013

Table 4.2: Comparison of sine-fit properties from analytic and experimental results

2. **Case 2: Amplitude** 10 **mm, Frequency** 2 **Hz, Added weight** 0 **kg,** 1 **kg,** 2 **kg**

After observing the above remarks, a different test case is chosen – 10mm amplitude and 2 Hz frequency. Extra weights of 1 kg and 2 kg are loaded onto the system, and a plot of the time signal is as shown in Figure 4.2 below. It is observed that the three scenarios match closely. However, on careful inspection of the signals, there exists some difference around the peaks. This difference in peaks cannot be immediately used to write off the motion system, due to the extra loading, as the final experimental setup would have added weight from the plunger filled with a volume of water.

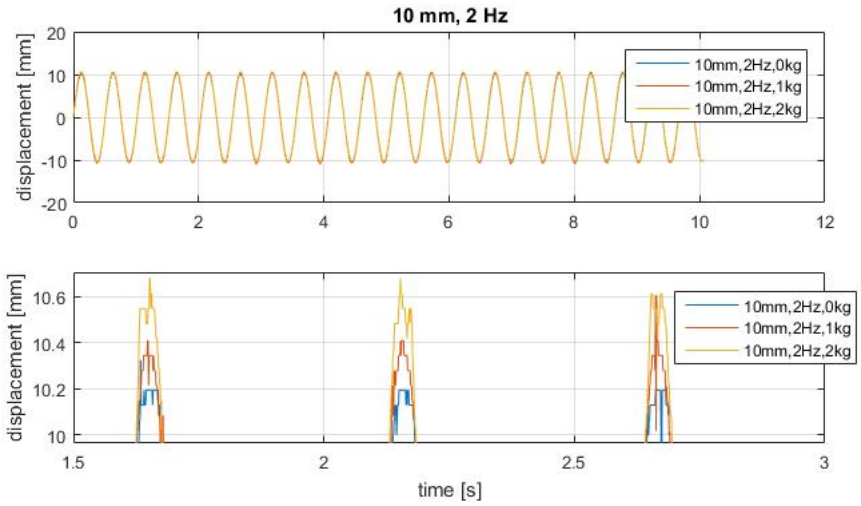

Figure 4.2: Displacment - time signal for different extra weights - Case 2

After fitting each of the time signals with a sum of 3 sines, there exists an *error* – a deviation of the time signals from the sine fit. A comparison of the deviations for the three load cases, as shown in Figure 4.3 below, shows that the magnitude of the deviation reduces as the load in the system increases. This is indeed desirable, as the final setup scenario would have significant load in the system, which would make the displacement-time signal approach the sum of sines. Table 4.3 shows this deviation in numbers.

Analyzing the signals with three load cases in the frequency domain shows that with more load (2 kg in this case) in the system has the largest amplitude - approaching the input amplitude of 10 mm (Figure 4.4). This high peak, having the "thinest" spectrum, simply means that most of the energy being put in the system is exhibited at the intended frequency (2 Hz) - which is desirable. Thus, it can be concluded that the motion enforcement gives better results when more weight is in the system.

Load [kg]	Deviation amplitude [mm]	Deviation as % of Osc. Amp-10mm
0	± 0.8	± 8%
1	± 0.7	± 7%
2	± 0.3	± 3%

Table 4.3: In numbers; deviations of time signal from sine fit - for varying loads in the system

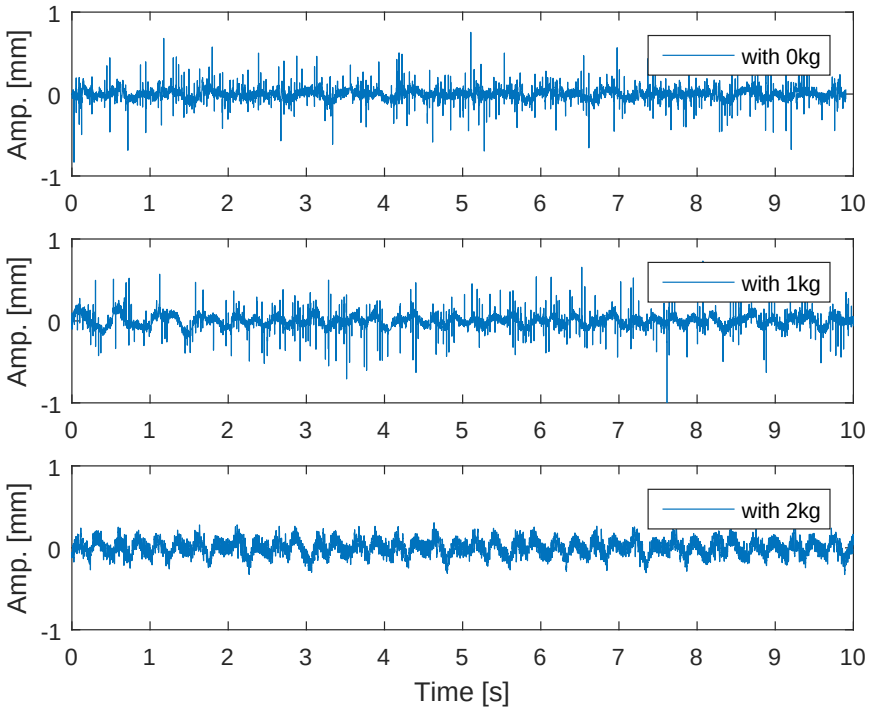

Figure 4.3: Deviations of time signal from sine fit - for varying loads in the system

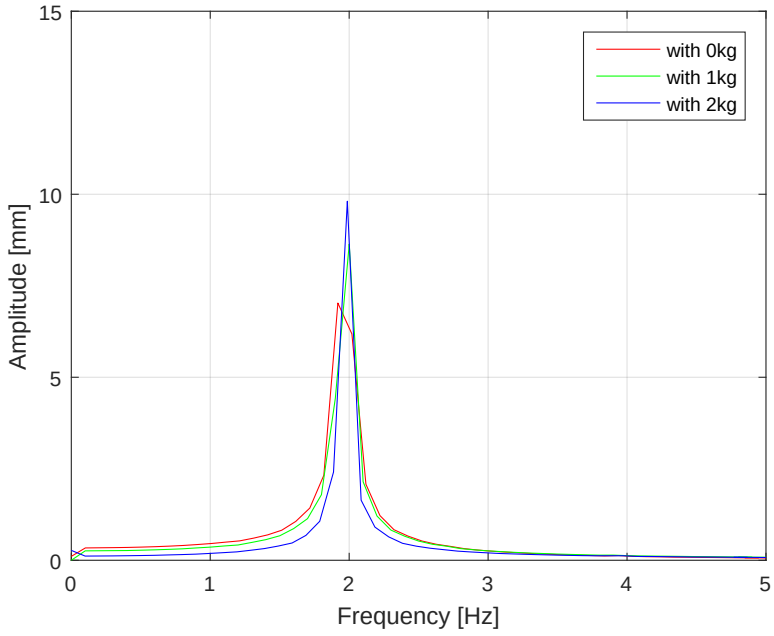

Figure 4.4: Single-sided amplitude spectrum of displacement, with varying extra loads

4.2.2. COMPARISON OF MEASURED MOTION DATA WITH KINEMATIC ANALYSIS

As noticed in the previous section, the ratio of amplitudes of the second and first harmonic in the sine-fit from the experimental motion data differs from that obtained in the kinematic computation analysis. As such, an investigation was made into the sensitivity of the ratio between the amplitude of the second harmonic (i.e. twice the input oscillation frequency) and the input amplitude to the size of the system. Size here referring to the crank radius and the connecting arm length. The crank radius translates directly to the oscillation amplitude. A ratio of this to the connecting arm length is the parameter investigated. Figure 4.5 below shows a linear relationship between the ratio of the third amplitude to the first amplitude and the system size. The ratio of the third amplitude to the first amplitude increases with increasing system size. From this, it can be seen that for the size of the system used in the physical experiment (amplitudes of 5, 10 and 15 mm, and connecting arm length of 0.5 m), a ratio of amplitudes resulting in less than 1% value is expected.

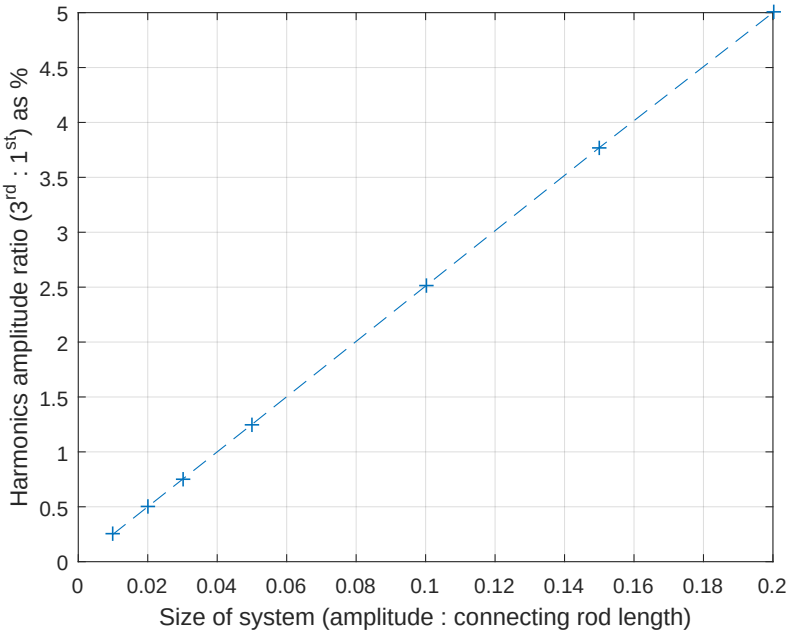

Figure 4.5: Sensitivity of 2^{nd} harmonic amplitude from sine-fit as a function of input amplitude to system size (oscillation amplitude : connecting arm length)

4.2.3. COMPARISON WITH RIZOS (2016)

With the study conducted by Rizos [1] being one of the motivations for this experimental thesis, the need to make comparisons between a key ingredient in both studies is necessary. This means comparing the motion signal data obtained from the displacement measurer in both cases. Fundamentally, the key difference is the use of a linear motor, as compared to a rotary motor in this study. For this comparison, key metrics to be employed would be frequency domain analysis (FFT) and time domain analysis. The parameters in the comparison are amplitude of 10 mm and frequency of 4 Hz.

Time Domain Comparison

By simply plotting the rigid body motion signals in time domain and comparing them shows that both methods give relatively similar plots. However, on close inspection of both signals, as in Figure 4.6 below, the peaks in the signal from Rizos' study show significant variations of about 0.2mm magnitude, when compared to that of the present study. Albeit, in the present study, for an input amplitude of 10 mm, the peaks in the graph - which are relatively steady - are significantly above 10 mm. This can be ascribed to the allowance in the bearings used in the motion system, discussed in Section 3.1.1.

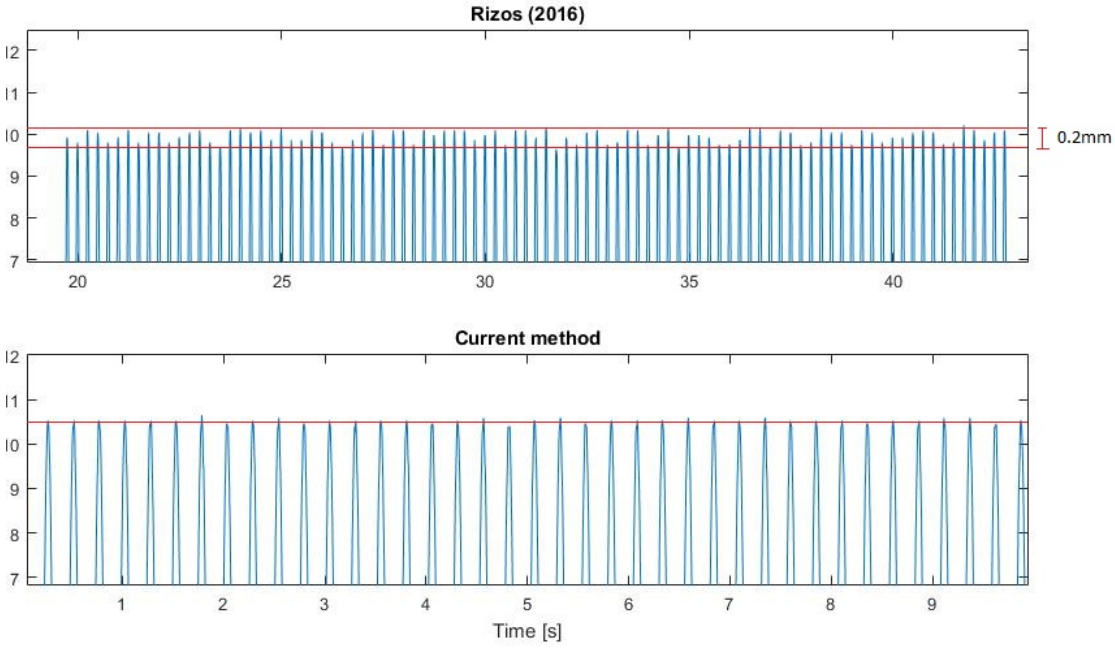

Figure 4.6: Time domain comparison of Rizos and current rigid body motion signals

Frequency Domain Comparison

Obtaining a Fast Fourier Transformation of both time domain signals as illustrated in Figure 4.7 below reveal some trends. At first glance, both plots appear quite similar, although the amplitude of the peak in Rizos is higher and thinner when compared to that from the current study. This can be attributed to a distribution of the input energy to other frequencies asides the input frequency. However, on closer inspection, as in Figure 4.7b, a lot of noise is seen in the plot from Rizos' study, with significant peaks at multiple integers of the base frequency. The noise in the lower frequencies is an unwanted phenomenon, as the response of the membrane is expected to be dominated by the lower frequencies. This frequency domain trend shows that Rizos' methodology proves to concentrate the input energy at the input frequency, but as seen from the time domain comparison, the amplitude enforcement of the methodology is not reliable.

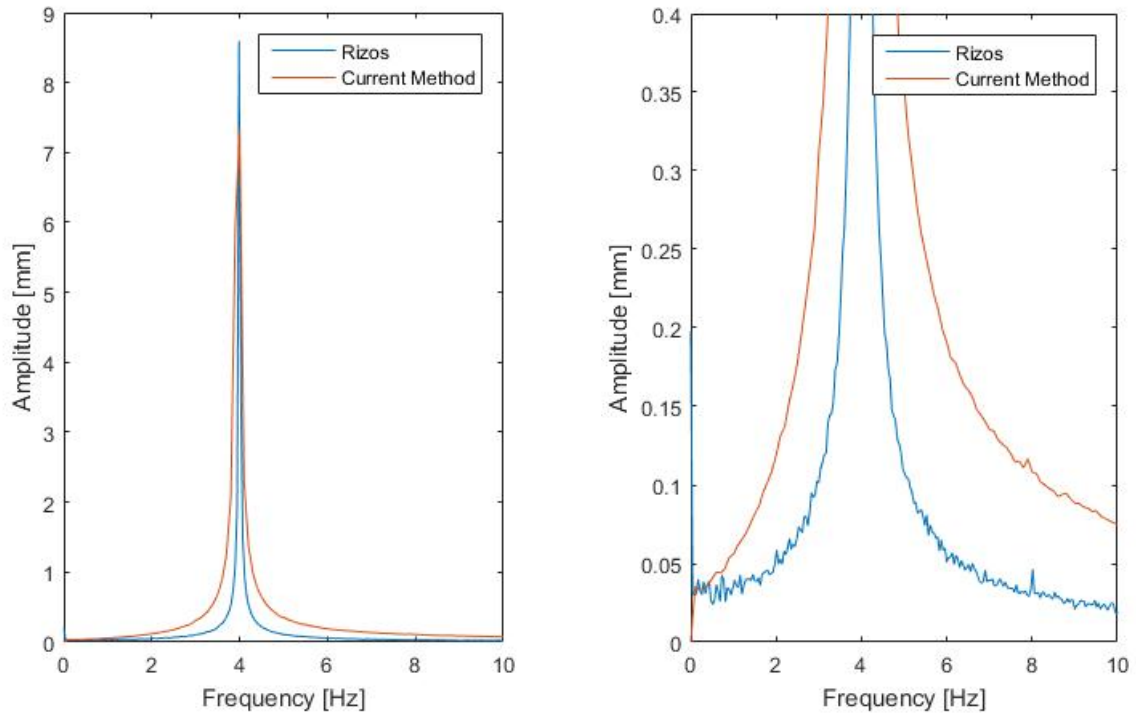

(a) normal view

(b) zoomed view

Figure 4.7: Frequency domain comparison of Rizos and current rigid body motion signals

4.3. SECOND EXPERIMENT - MEMBRANE VIBRATION ANALYSIS

After finalizing the experimental setup, ensuring that all the different aspects function satisfactorily, experiments are conducted based on cases and parameters pre-informed by various factors. These influencing factors are discussed below, and the results from selected scenarios are analysed and reported.

4.3.1. CASES INVESTIGATED

As already established that large deflections of the membrane during the experiments are intended, the cases investigated had to be modified. These cases have parameters which include varying water volumes, frequencies and amplitudes; and single point measurements carried out at the centre of the membrane and at locations of half of the radius over a 180 degree range, with a step of 30 degrees. Reasons for the decision to alter the parameters are listed below:

- The water volume, which directly corresponds to the water column above the membrane, is selected to prevent water coming out of the plunger during motion enforcement.
- High frequency motions cause severe sloshing, at higher water columns in the plunger; which is not desirable in these experiments
- Severe sloshing resulting in a loss of water from the plunger makes the water volume in

the cylinder change, which compromises the experiment intentions. Splashes of water during severe sloshing, also ruins measurements from the triangulation laser displacement measurers beneath the setup, in addition to having a tendency of ruining the devices.

Due to the undesirable and/or intended effects outlined above, the experimental matrix is adjusted, with cases presented below. The reasoning behind selecting these cases was that all types of parameters had to be included. Moreover, visual observation during the execution of experiments, also, determined the choices made. The cases are investigated as summarized in Table 4.4 below.

Case Nr.	Water Volume [ml]	Corresponding Water Height [mm]	Frequencies [Hz]	Amplitudes [mm]
1	50	10	4, 4.2, 6.4	10
2	100	19.9	4, 4.2	10
3	150	28.9	2.9, 4	10, 15
4	400	79.6	3, 4	10

Table 4.4: Investigated cases

4.3.2. FFT ANALYSIS

To analyze the vibrations of the membrane, Fast Fourier Transformations are utilized. However, based on the method of acquiring the deflections of the membrane (Section 2.4), a subtraction of the rigid body motion signal from the signal obtained from the motion of the membrane is needed. After this subtraction, the resulting signal, which is primarily that of the membrane response, is then transformed to the frequency domain. Some representative cases are presented.

1. **Case 1:** 50 **ml, A**=10 **mm, f**=4 **Hz**

   The case with 50 ml of water being put in the plunger, and then oscillated with an amplitude of 10 mm and frequency of oscillation of 4 Hz is analysed in the frequency domain, as shown in Figure 4.8. It can be seen that the motion of the membrane is dominated by the frequency of the imposed motion, as there exists the biggest peak at same frequency. Also, peaks at about integer multiples of the imposed motion frequency are present.
   The amplitudes of the peaks obtained from the frequency domain analysis (Table 4.5), are compared. One interesting feature seen is that the 2nd multiple peak (i.e. the peak at thrice of the input frequency - ~ 12 Hz) is larger than the peak at twice of the input frequency. However, nothing can be said about this for now, until other scenarios are analysed and compared.

2. **Case 3:** 150 **ml, A**=15 **mm, f**=4 **Hz**

   Similar analysis to the case above is carried out on Case 3, with an amplitude of 15 mm and a 4 Hz frequency of oscillation (Figure 4.9). Here, it can be seen that apart from distinct peaks at the input frequency and integer multiples of this, there are also

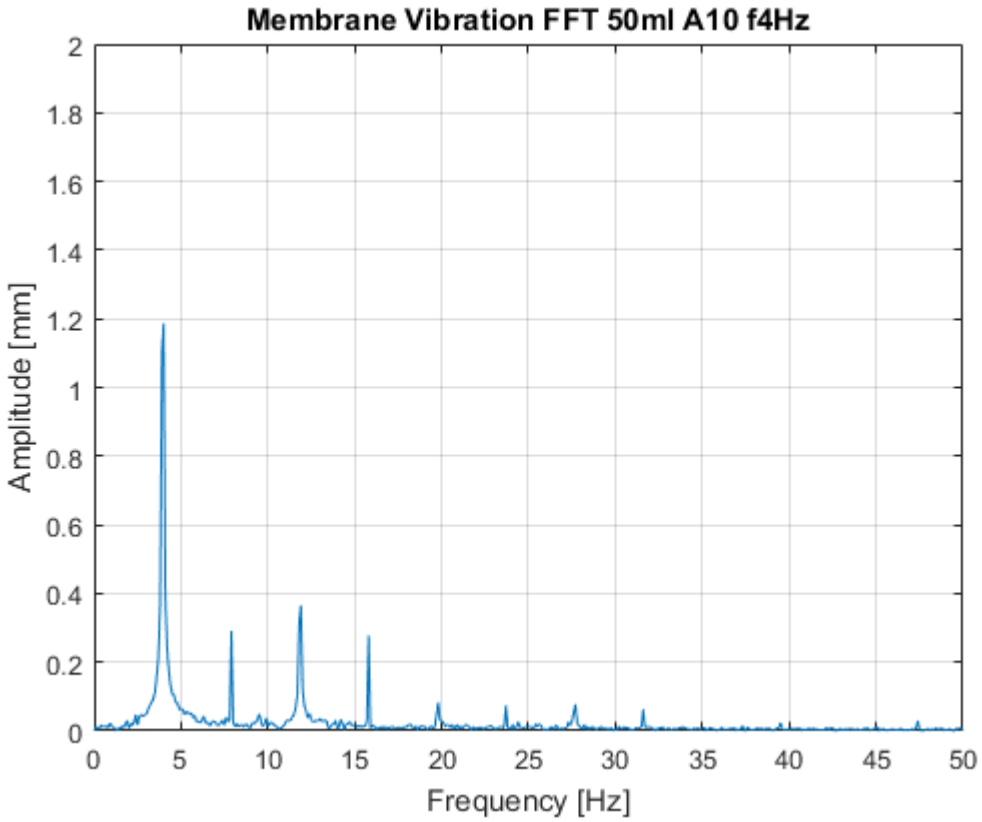

Figure 4.8: FFT of Case 3 with 50ml of water, Amplitude = 10mm and Frequency = 4Hz

50ml, A10mm, 4Hz	Peaks			
	1st	2nd	3rd	4th
Frequency [Hz]	4	7.9	11.9	15.8
Amplitude [mm]	1.187	0.2916	0.3655	0.2777
Amp. as % of 1st peak		24.57%	30.79%	23.4%

Table 4.5: Comparison of amplitude of peaks from FFT - Case 1

numerous peaks similar to a noise signal, all within the region of the first four standout peaks, but with amplitudes less than 0.5 mm. This phenomenon, which is absent in the previous case analysed, could be as a result of more motion (sloshing) of the water in the plunger during excitation, resulting from a higher amplitude of oscillation coupled with a higher column of water being in the plunger. As such, more motion in the water excites the membrane more and at intermediate frequencies, but not as much as the excitation resulting from the driving frequency.

A comparison of the amplitude of the peaks is as given in Table 4.6 below. It is seen that the first integer multiple peak (i.e. ~ 8 Hz) has the greatest amplitude of all the integer multiple peaks, contrary to the second integer multiple peak obtained in *Case* 1. However, similar to Case 1 analysed earlier, the second integer multiple peak has an amplitude that is about 30% of the amplitude of the peak at the input frequency.

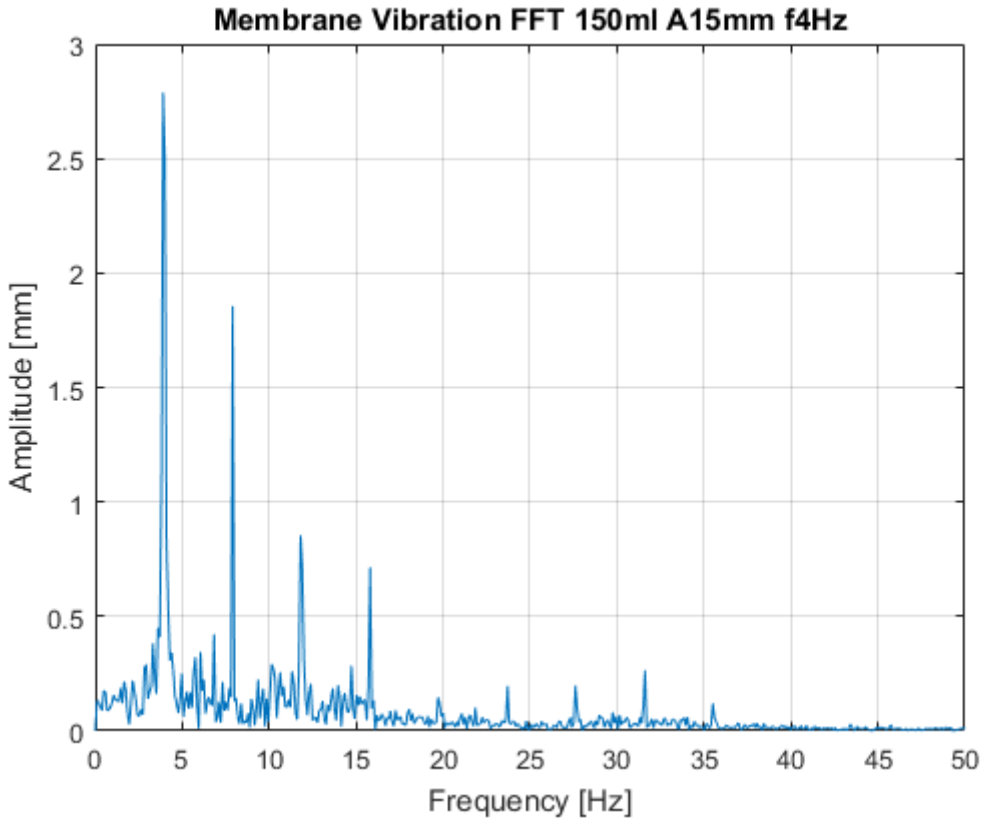

Figure 4.9: FFT of Case 3 with 150ml of water, Amplitude = 15mm and Frequency = 4Hz

150ml, A15mm, 4Hz	Peaks			
	1st	2nd	3rd	4th
Frequency [Hz]	3.9	7.9	11.81	15.8
Amplitude [mm]	2.788	1.855	0.854	0.7135
Amp. as % of 1st peak		66.54%	30.63%	25.59%

Table 4.6: Comparison of amplitude of peaks from FFT - Case 3

3. **Case 4 -** 400 **ml, A=**10 **mm, f=**3 **Hz**

Keeping the amplitude at 10 mm but reducing the frequency to 3 Hz, with significantly more volume of water - translating to more water column above the membrane, it can be seen from Figure 4.10 that the response of the membrane is majorly dominated by a frequency component at the motion input frequency (i.e. 3 Hz). A comparison of the amplitudes of the peaks at integer multiples of the input frequency (Table 4.7) illustrates that.

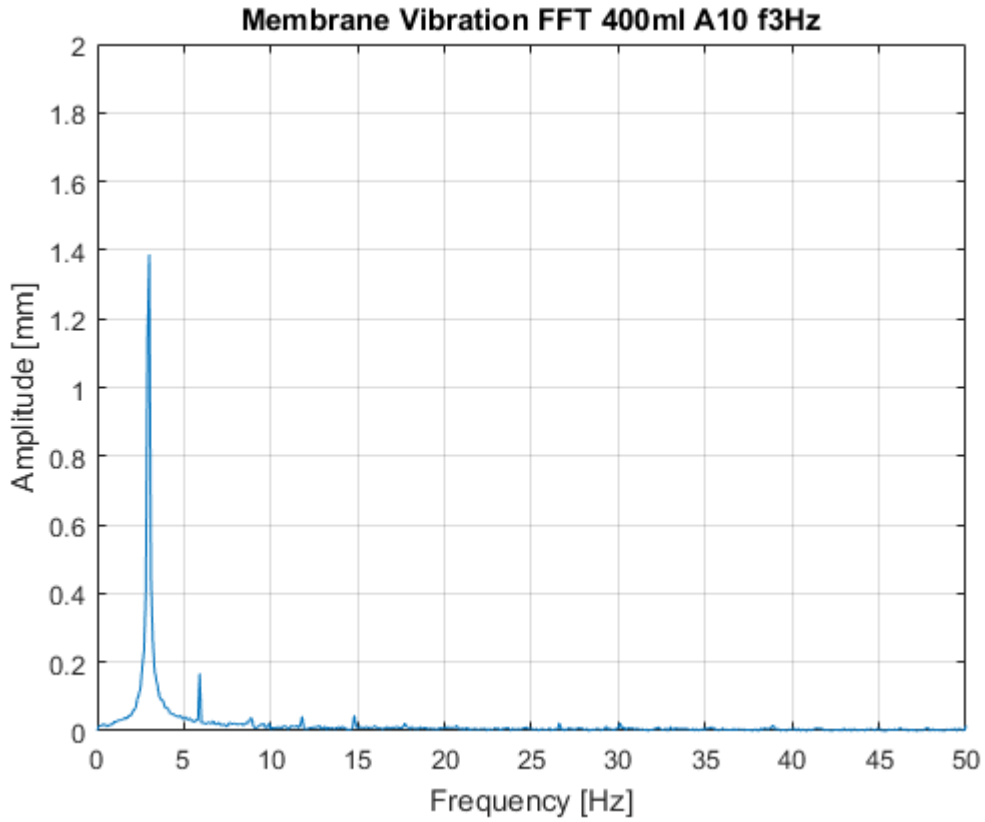

Figure 4.10: FFT of Case 4 with 400ml of water, Amplitude = 10mm and Frequency = 3Hz

400ml, A10mm, 3Hz	Peaks			
	1st	2nd	3rd	4th
Frequency [Hz]	3	5.9	8.8	11.8
Amplitude [mm]	1.378	0.1666	0.0363	0.0418
Amp. as % of 1st peak		12.09%	2.63%	3.03%

Table 4.7: Comparison of amplitude of peaks from FFT - Case 4

Based on the above three representative cases analysed, it is difficult to come to make a conclusive remark about the sensitivity of the membrane response to the input parameters. To draw out a trend in the membrane response behaviour, two dependencies are treated - Volume dependence and Frequency dependence, in addition to analysis of polar measurements.

4.3.3. FREQUENCY DEPENDENCE

To really understand the membrane response during FSI experiments and to be able to predict the behaviour in response to varying parameters, a frequency dependence is investigated. For all the four cases (Table 4.4), the frequency domain response of the membrane is analysed, keeping the water volume and amplitude constant per case. The result, as shown in Figure 4.11, shows in all cases, when the frequency of oscillation is increased to 4 Hz (or slightly above 4 Hz), there is an increase in the amplitude of the first peaks.

Interesting to note, as seen from Case 1 - with 50 ml of water volume and 10 mm oscil-

lation amplitude, is that there is an increase in the deflection amplitude as the oscillation frequency is increased. However, there is a dip at about 4.8 Hz, before picking up and having the maximum peak corresponding to an oscillation frequency of 5.5 Hz. This frequency can be thought of as one of the natural frequencies (invariably the first natural frequency) of the membrane in this coupled system. This, however, cannot be verified from experiments in other cases, as increasing the frequency with more than 50 ml of water in the plunger results in severe sloshing - which makes it rather impracticable to conduct experiments and/or measurements. Also noticeable is that the second peaks of oscillation frequencies 6 Hz and 6.4 Hz are significantly large - ~ 72% and ~ 85% respectively of their first peaks.

4.3.4. VOLUME DEPENDENCE

To investigate the membrane response to a variation in volume of water in the plunger, different experiments were conducted, keeping the amplitude and frequency of oscillation constant - at 10 mm and 4 Hz respectively, while varying the amount of water in the plunger. Also, more experiments were conducted with an increased frequency (4.2 Hz), but cases with more than 100 ml of water (Figure 4.13) in the plunger could not be carried out due to practical reasons, as there was severe sloshing leading to loss of water from the plunger and likelihood of damaging the measurement equipment.

The frequency analysis of the volume variation at 4 Hz shows that for an increasing volume of water in the plunger, there is an increasing amplitude of the response at the input frequency. However, when the frequency in increased to 4.2 Hz, for an increasing volume of water, there is a decreasing amplitude. See Figures 4.12 and 4.13.

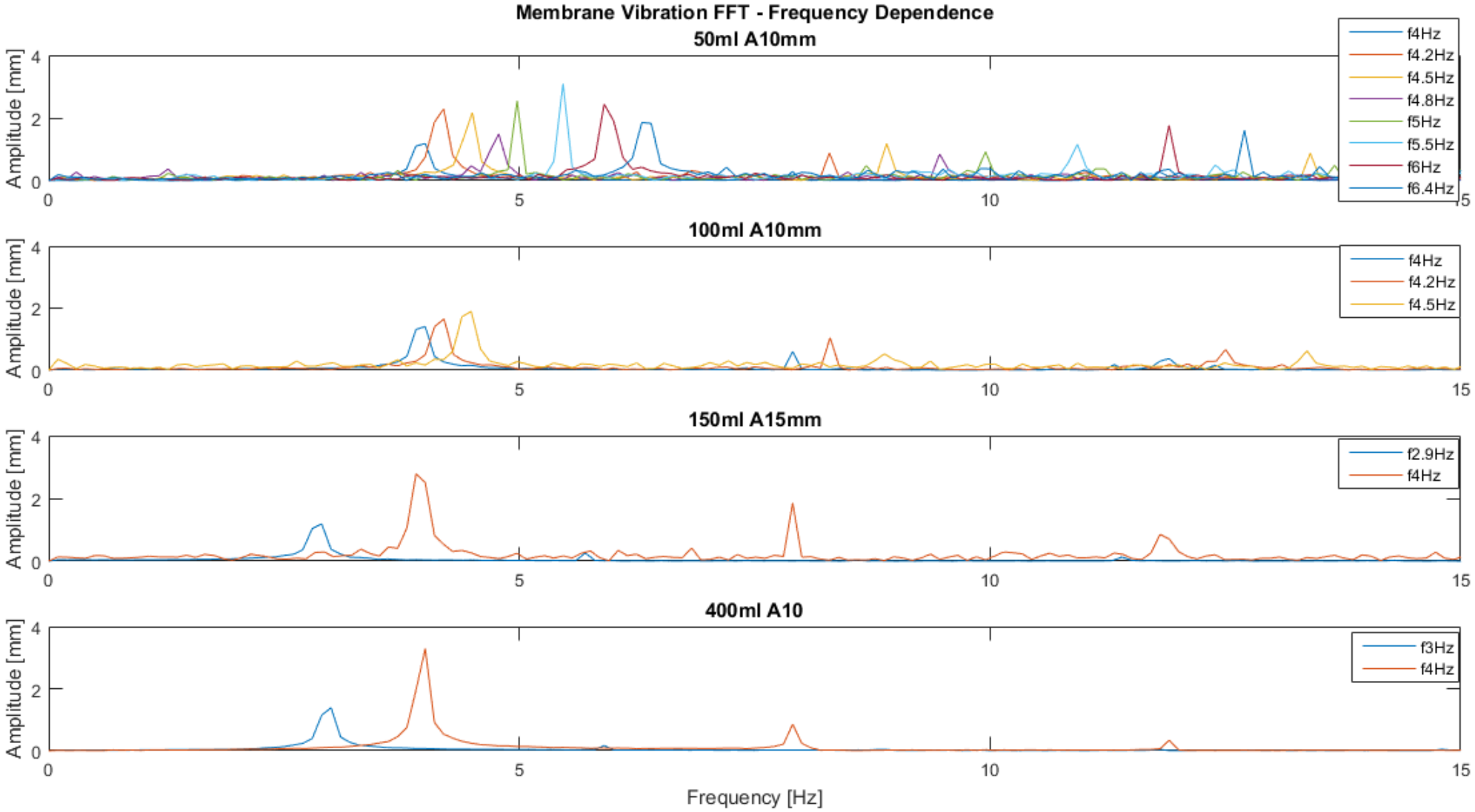

Figure 4.11: Dependence of membrane response on frequency variation

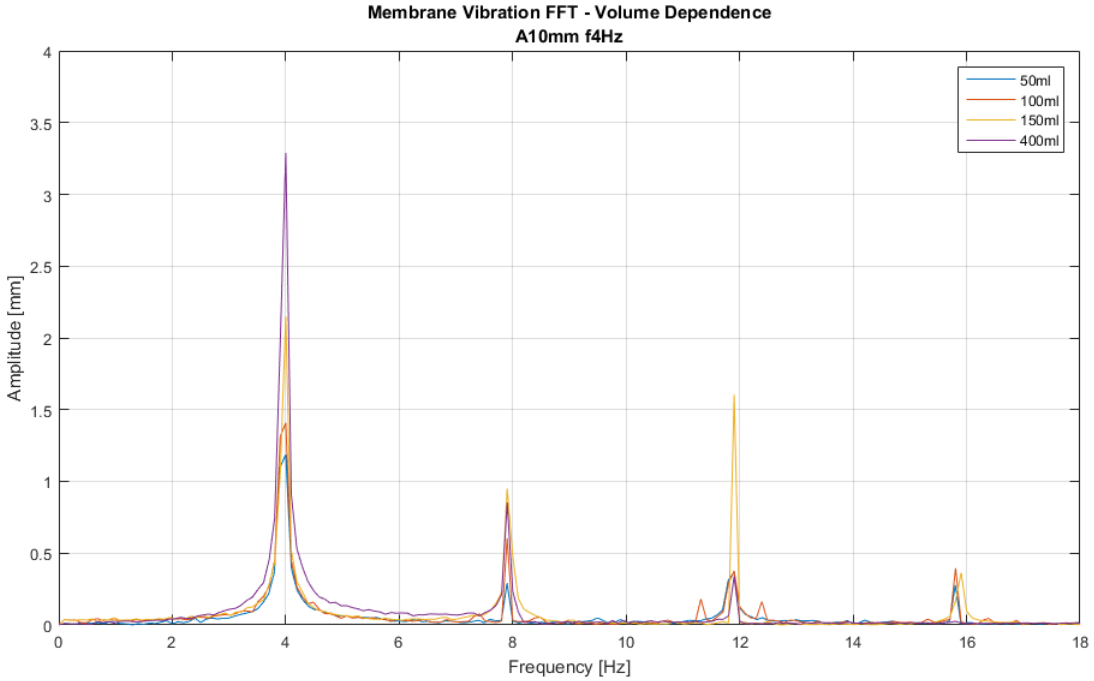

Figure 4.12: Dependence of membrane response on volume variation for A10 mm, f4 Hz

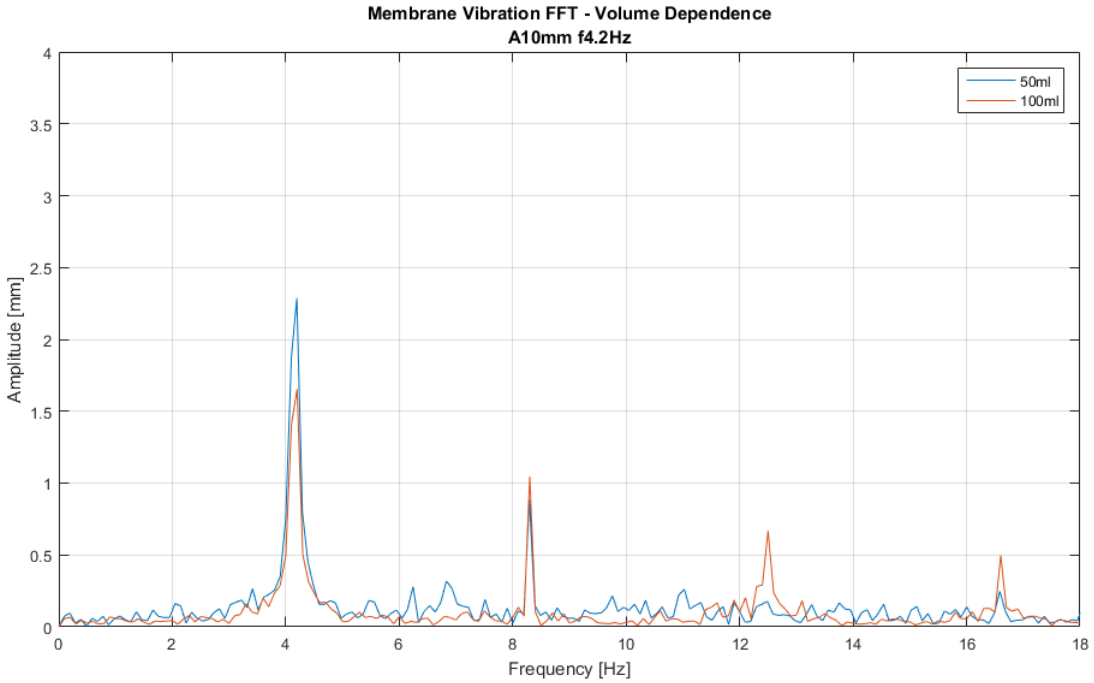

Figure 4.13: Dependence of membrane response on volume variation for A10 mm, f4.2 Hz

4.3.5. POLAR ANALYSIS

Based on the approach of measurement of the membrane vibration, polar measurements were also taken (see Figure 2.8), and are then analysed; as the imposed motion of the plunger-water system is aimed at exciting the fundamental mode of the membrane, which is expected to give significant deflections at half radius. Measurements obtained at the said polar locations are analysed in the frequency domain for two representative cases as shown in Figures 4.14a and 4.14b below. Only the first peaks in the frequency plot of each of the angular points are considered, as they possess the largest deflection in each frequency analysis.

From the analysis, it is seen that the amplitude of the deflection at the centre of the membrane is clearly the largest. This is however unexpected, as the centre of the membrane is expected to be a node, as a nodal diameter passes through it. However, an explanation for this trend is that the deflection measured at a certain frequency, could in reality, be a summation of multiple modes; as the coupled frequency behaviour of the membrane is not known, for certain, beforehand. In addition to this trend, it is also noticeable that the deflection peak at $theta = 150°$ for both cases of 50 ml and 400 ml of water analysed with oscillating frequencies of 4.2 Hz and 4 Hz respectively, shows a significant surge above the neighbouring peaks.

This trend gives the indication of a possible mode shape that could be associated with this patter. However, the current experimental setup cannot provide full membrane surface measurements to verify this. As such, only further experiments involving scanning measurement equipment can reveal any possible mode shape. The Polytec scanning vibrometer is one of such equipment.

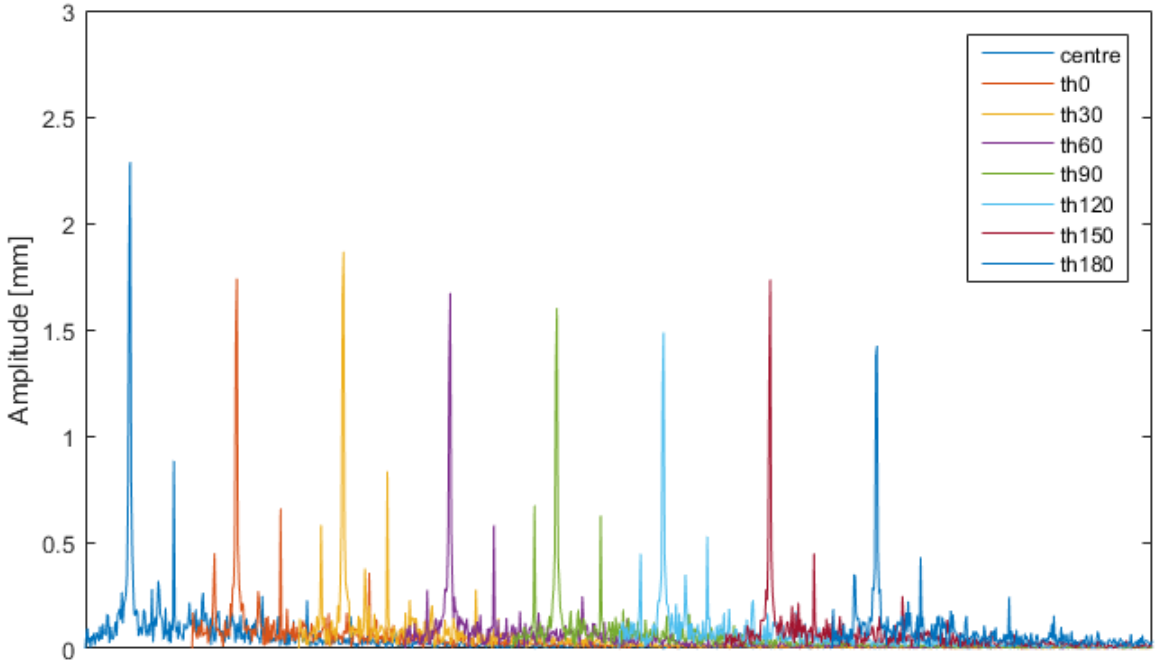

(a) 50 ml, A10 mm, f4.2 Hz

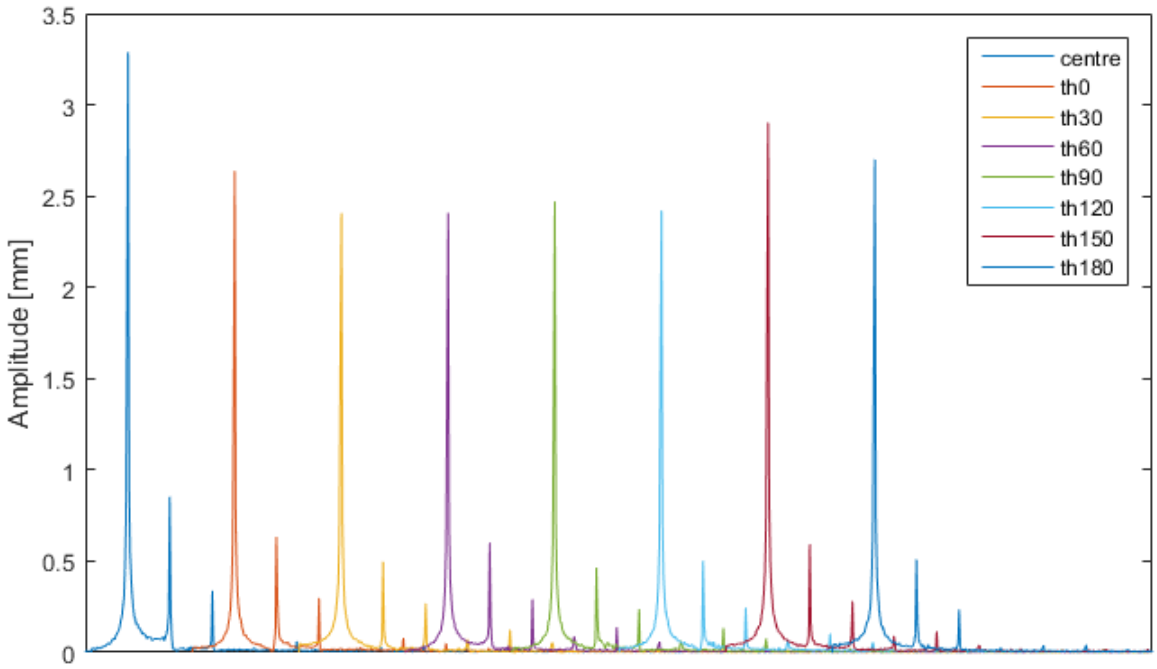

(b) 400 ml, A10 mm, f4 Hz

Figure 4.14: FFT Membrane response at location r/2 across a 180° range, with a 30° step - shifted on the x-axis for clarity. Deflection at centre is plotted for reference

5

ERROR ANALYSIS

5.1. INTRODUCTION

In experimental research, the need to account for uncertainties cannot be overemphasized; not just the type that can be assessed by statistical analysis based on repetition of measurements – random uncertainties, but also those which cannot – systematic uncertainties. As errors are never really known *exactly*, this chapter attempts to identify and discuss in detail the different sources of error arising in the experimental setup/procedures, and then estimate them. Since random errors are not considered in this study, due to no repetition of experiments to ascertain the said random errors, this leaves the major sources of error in the experiments as systematic and uncertainties from calibrations.

5.2. SYSTEMATIC UNCERTAINTIES

Systematic uncertainties are introduced as inaccuracies inherent in the experimental system, and they usually come from measuring instruments. Tracking down sources of systematic errors is difficult, and often never completely exhaustive. For the experimental setups, the source of systematic errors is mainly from the laser triangulation displacement measurer, which is discussed in the following paragraphs.

5.2.1. LASER TRIANGULATION DISPLACEMENT DEVICE

The systematic errors arising from this measurement device can be put under two categories:

1. Zero setting error

   This error is seen when the instrument is used to measure a stationary surface, with the expectation of a zero or fixed reading. However, the signal obtained oscillates between a relatively constant range. This can be attributed to the maximum resolution of the displacement measurement system, as discussed in the following paragraph.

Maximum resolution of RBM measurement system

The RBM measurement system consists of a laser triangulation displacement device (technical specifications in the table below) connected via a junction box having a resistance of $0.488k\Omega$, to a *National Instruments* (NI) 12-bit USB-6008 data acquisition (DAQ) box. A USB connection from the box to a computer, enables the output of the measurement device to be obtained, via a LabView program. As seen in table 2.1, the triangulation displacement device has an output range of 4 mA - 20 mA. This, when combined with the $0.488k\Omega$ resistance from the junction box, gives upper and lower voltages of 9.76 V and 1.952 V for 20mA and 4mA respectively, resulting in an output voltage range of 7.808 V. The DAQ box has its own input range of 10 V, which when combined with its 12bit converter yields about 2.44 mV/bit.

Upon combination of the volt-per-bit rating of the DAQ and the output voltage range of the displacement measurer, a measuring step value of 3198 bits is obtained. The displacement measurer has a measurement range of 100 mm, which when combined with the measurement step of 3198 bits earlier obtained, results in a resolution of 31 micrometers per bit. This resolution can be seen in the measurements obtained when the laser triangulation displacement measurer is focused on the lapped steel pointer of a Height Measuring and Scribing Instrument; DIgimar 814SR – which is a highly calibrated accurate device, with accuracy of 10 microns. The measurement reading from the triangulation device gives a resolution/error of about ±33 microns.

2. Multiplier error

   The multiplier error can be noticed when a quantity is constantly measured to be more than what is specified. Most susceptible to this type of error are the amplitudes of oscillation. To account for this, the amplitudes of oscillation, which are already predefined as slots off-center on a disc, are measured.

Oscillation amplitude verification

After obtaining the maximum resolution, or in other words – the highest accuracy, of the RBM measurement system, the next step in the experimental procedure would be to accurately verify the proposed amplitudes of oscillation. To do this, the top flange of the plunger is bolted to the bottom of the connecting rod, whose top end is connected to slots on a circular member, via a sliding bearing. These slots correspond to the different amplitudes, that are drilled off-center. Motion is applied per amplitude. The laser triangulation displacement measurer is used to measure this motion, by placing it on a board directly above the plunger, pointing downward at the flange. To accurately obtain the amplitude measurements, the plunger must be oscillated, per amplitude, as smoothly as possible. It is important to ensure that no inertial effects are present in the motion enforcement. As such, the motor is fed with a frequency of 2 Hz via the linear drive, which directly translates to $\frac{1}{3}$ Hz due to the $6:1$ gear reduction system. Upon subjecting the analogue output of the triangulation displacement device to signal filtering, the motion measurements obtained are analyzed thus. Figure 5.1 below shows a time plot of the signals from each of the amplitudes. Based on the already verified

curve fitting scheme (See appendix A), the amplitudes in each case is measured, and the error (deviation) is as summarized Table 5.1 below.

Amplitude Intended [mm]	Amplitude from sine-fit [mm]	Absolute (Uncertainty) [-]	Uncertainty (Relative) [%]
5.00	5.181	0.181	3.62
10.00	10.328	0.328	3.28
15.00	15.025	0.025	0.17

Table 5.1: Uncertainties in imposed amplitudes of oscillation

The errors in the amplitudes as obtained from the comparison with a sine-fit, shown in Table 5.1, would then have to be summed with the uncertainties resulting from the maximum resolution of the RBM measurement system (±0.033 mm). This would result in uncertainties of 0.217 mm, 0.361 mm and 0.058 mm in the amplitudes of 5 mm, 10 mm and 15 mm respectively.

5.3. CALIBRATION UNCERTAINTIES

As already established that for experimental procedures, obtaining measurements with known accuracies is necessary. In line with achieving this, there is need to correlate the readings of measurement devices to be used, with those of a standard, in order to check/obtain the instrument's accuracy; or in some cases, derive a transfer function. Below, the steps taken to calibrate each of the devices are explained.

5.3.1. FORCE TRANSDUCER

The force transducer, based on its principle of operation, gives a voltage output. Because this output voltage is quite small, there is need to pass it through an amplifier, and being an analogue signal, pass it through a filter as well. To calibrate the force transducer, it is loaded with standard known masses, both in tension and in compression, as in figure 5.2 below. In tension (figure 5.2b), the transducer is fixed to the setup and a hanger is attached to the bottom, which is then loaded. Alternatively, in compression (Figure 5.2a), rectangular plates are attached to the ends of the transducer, before being loaded with the known masses. For both cases, the voltage reading on the amplifier is zeroed before loading the transducer with any mass. The result of the calibration is shown in the figure below, whose points when fitted with a curve, give the Equation 5.1. This equation indicates the transfer function (sensitivity) of the force transducer.

$$\text{Force} = 9.745 * \text{Volts} - 0.6587 \tag{5.1}$$

$$\text{Slope} = 9.745 \pm 0.106 \ \frac{Newton}{Volt}$$
$$\text{Intercept} = -0.6587 \ \pm 0.2996$$
$$\text{SSE} = 9.069$$

The coefficients of the straight-line fit in Equation 5.1 are obtained by using the *Curve Fitting Toolbox* applet from MATLAB R2015b, and the slope and intercept values are given with a 95%

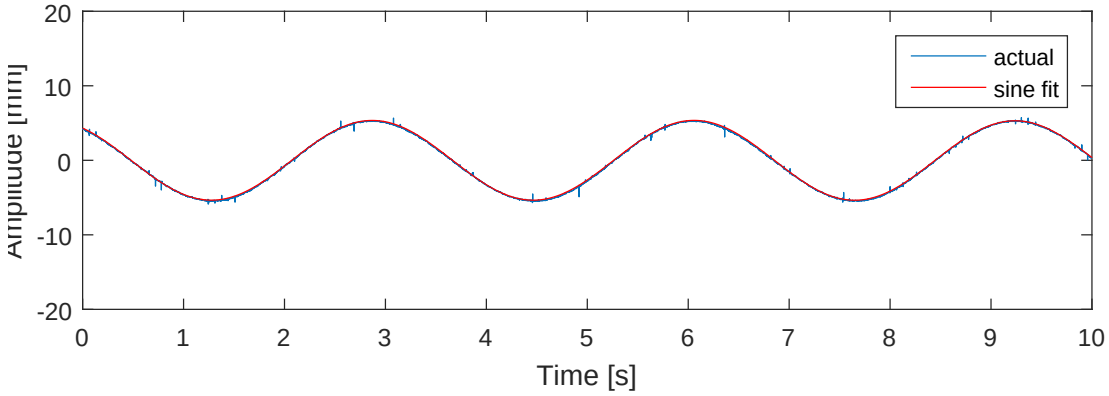

(a) 5 mm

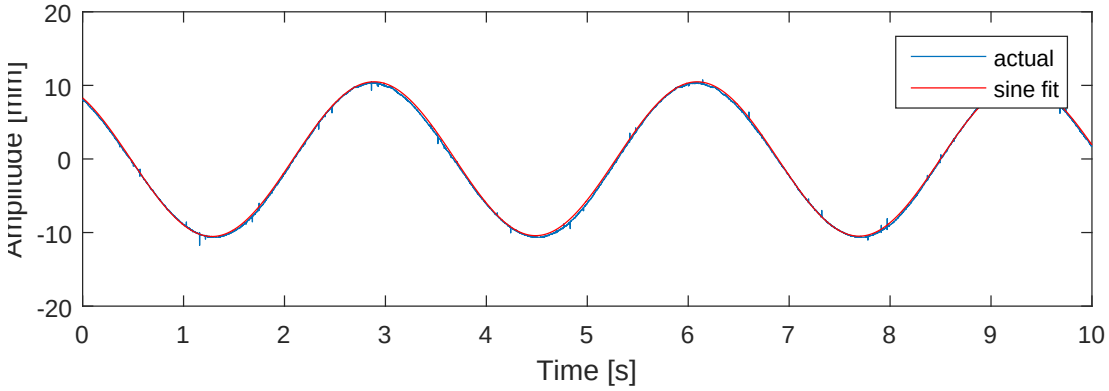

(b) 10 mm

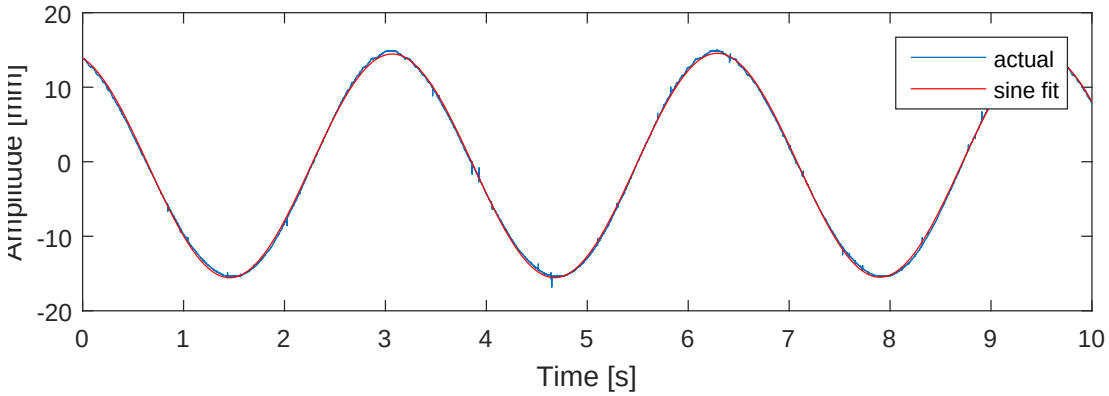

(c) 15 mm

Figure 5.1: Amplitude verification plots, fitted with sin fits

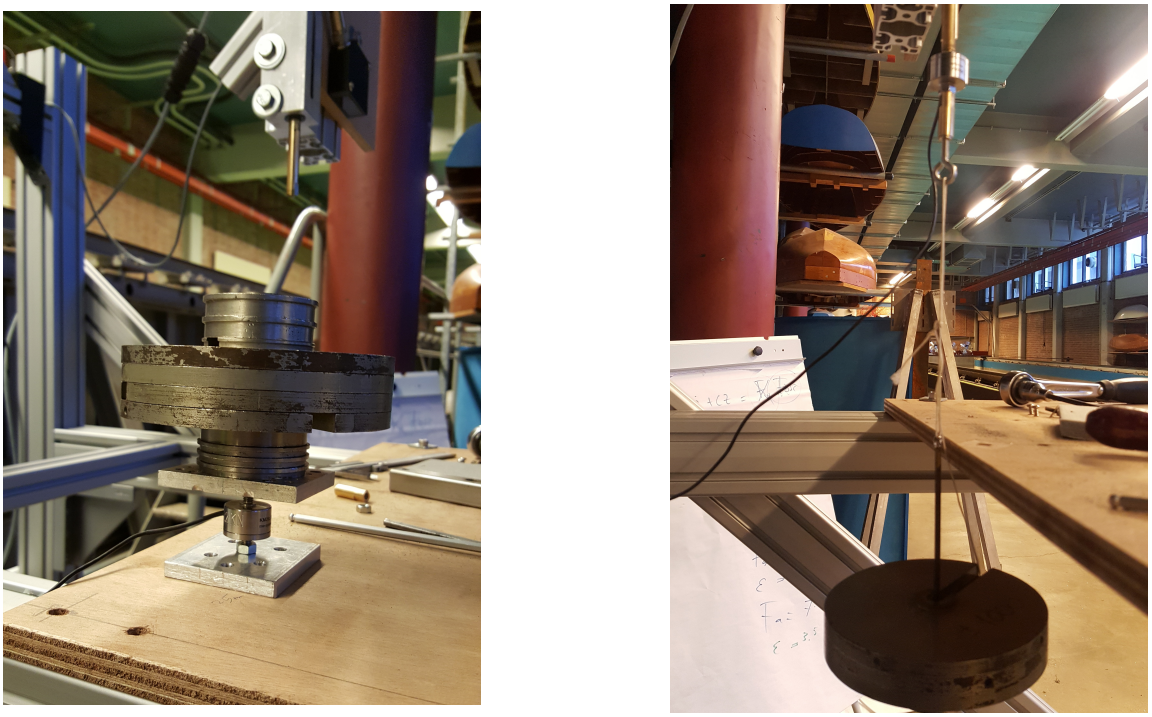

(a) Compression

(b) Tension

Figure 5.2: Force transducer loaded with weights for calibration

confidence having the following *Standard-Errors* (uncertainty) as shown. A statistic measure (Sum of Squares due to Error (SSE)) is used to obtain the total deviation of the response values from the fit to the response values, defined mathematically in Equation 5.2. The SSE uses a model that relates the response data to the predictor data with one or more coefficients, which results in an estimate of the "true" but unknown coefficients of the model - which are obtained by minimizing the summed square of residuals.

$$\text{SSE} = \sum_{i=1}^{n} w_i (y_i - \hat{y}_i)^2 \tag{5.2}$$

where y_i = observed response value

$\hat{y}_i$ = fitted response value, and

w_i = weight assigned to each residual $(y_i - \hat{y}_i)$

5.3.2. LASER TRIANGULATION DISPLACEMENT MEASURER

Still in a bid to obtain results that are as accurate as possible, it is sought after to assess the laser displacement measurer to ascertain any inherent uncertainty in the measurement values given by the device. For this purpose, a Height Measuring and Scribing Instrument (Digimar 814SR); which is a more accurately calibrated length measurement device, is used. The displacement measurer is focused on the scriber of the height measurer, and then the scriber is displaced with known distances via the control knob, as in Figure 5.4 below.

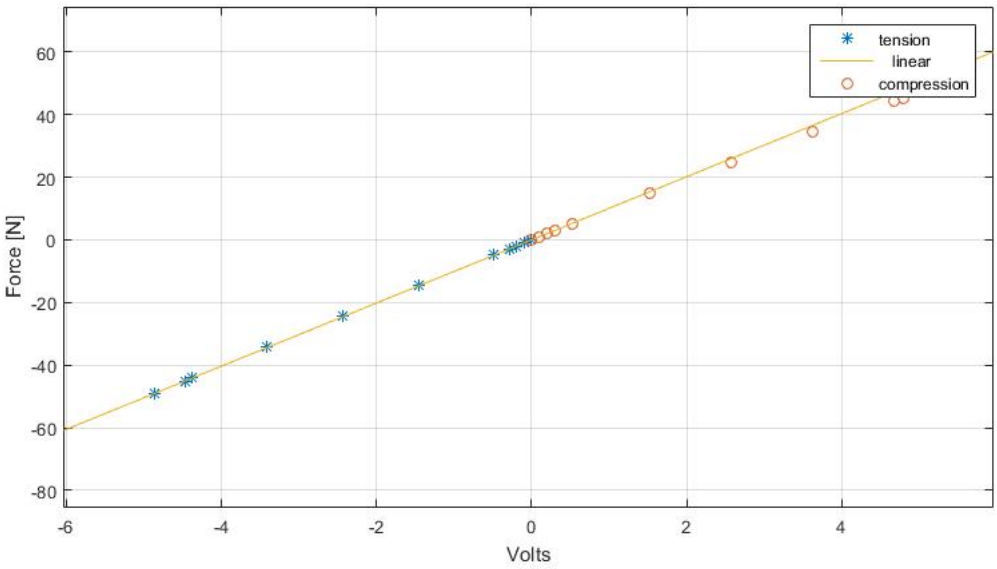

Figure 5.3: Force transducer calibration results, with a straight-line fit

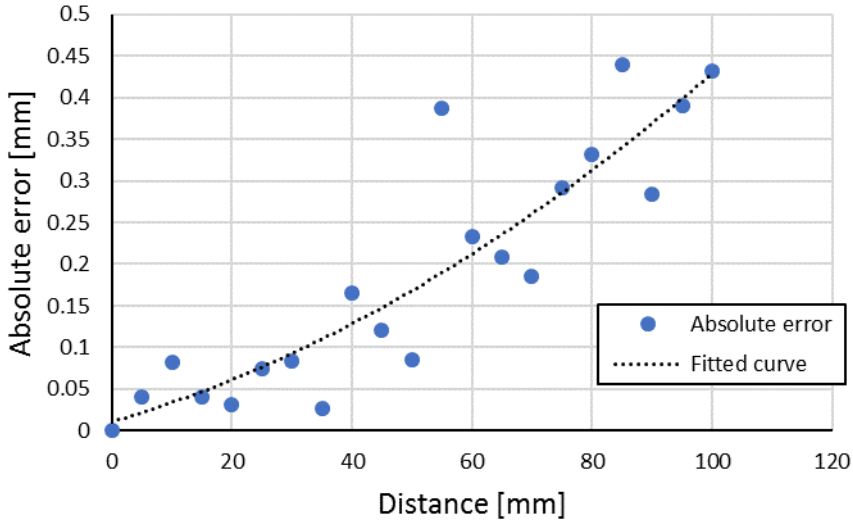

Figure 5.5: Plot of the error function derived from calibration of the laser triangulation displacement measurer, with a curve fit

By doing this, the absolute error in the laser displacement measurer is obtained, via the formula below:

$$\text{Absolute Error} = |\text{M} - \text{D}| \tag{5.3}$$

where M = Measurement from displacement measurer, and

D = Input distance from height meter

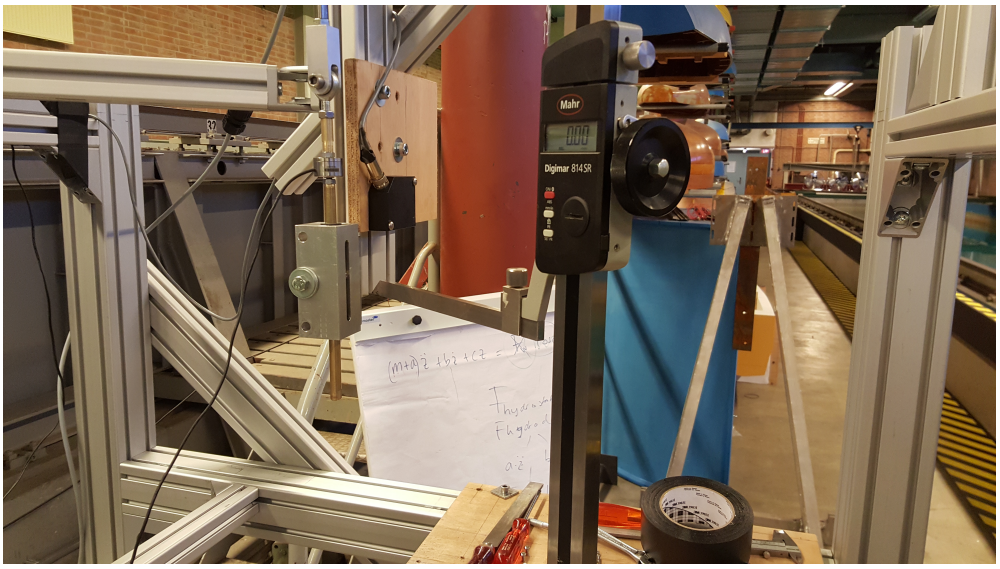

Figure 5.4: Digimar 814SR height meter used to calibrate the laser triangulation displacement measurer

This error function (Equation 5.3) is as plotted in Figure 5.5 below, as a function of distance. A trend can be noticed from the error plot, which illustrates that the magnitude of the error increases with increasing distance from the laser head.

From the curve fit of the absolute error data points done with the MATLAB *Curve Fitting Toolbox* applet,

$$SSE = 0.08308$$

Hence, this error value first needs to be added to the error in the height meter as specified by the manufacturer (Table 5.2), and then summed with the zero-setting error of the laser triangulation displacement measurer to obtain the total error in the displacement measurements.

Digimar 814 SR Specifications	
Measuring range	600 mm
Resolution	0.01 mm
Error limit	0.05 mm
Weight	8 kg

Table 5.2: Height measurer Digimar 814 SR technical data

5.4. OTHER SOURCES OF UNCERTAINTIES

With the primary sources of uncertainties in the experiments treated, there are however some errors that cannot be accounted for numerically. Uncertainties from these sources, however small they may be, still have to be outlined.

1. Allowance for movement in bearings, inherent in design.
2. Frequency enforcement from variable frequency control drive.

5.5. SUMMARY

With all the potential error sources identified and most of them quantified, a combination of the errors has to be done. The equipment used to obtain measurements relating to the rigid body motion and the membrane motion (vibration) being the same – laser triangulation displacement device, makes the error summation straightforward. An overview of the errors are given in table 5.3 below, and then summed using the quadrature principle.

Systematic errors per amplitude		Calibration errors from sources	
5 mm	0.181 mm	Triangulation device	0.45 mm
10 mm	0.328 mm	Digimar specified error	0.05 mm
15 mm	0.025 mm	Zero setting error	0.033 mm

Table 5.3: Summary of systematic and calibration uncertainties in measurements

Using quadrature,

$$\begin{aligned}\text{Total calibration error} &= \sqrt{\text{Triangulation}^2 + \text{Digimar}^2 + \text{Zero setting}^2} \\ &= \pm\, 0.45\text{mm}\end{aligned}$$

Now, total error per amplitude,

$$\text{Total error} = \sqrt{\text{Total calibration error}^2 + \text{Systematic error}^2}$$

Table 5.4 below gives the accuracy of the system per amplitude.

Amplitude [mm]	Total error (absolute) [mm]	Total error (relative) [%]
5 mm	± 0.485	± 9.7
10 mm	± 0.557	± 5.57
15 mm	± 0.451	± 3

Table 5.4: Summary of total uncertainties per amplitude

6

CONCLUSIONS AND RECOMMENDATIONS

Experiments have been conducted, with results and analysis of some representative cases presented in chapter 4. Error estimates of the experimental procedures have also been done and reported. From the results of the experiments, conclusions and recommendations are presented in this chapter. The conclusions aim at answering the thesis objective while recommendations are provided to give insights into furthering the experiments, should there be an extension of the current study. The thesis objective was to provide validation data for a computational tool being developed through experiments which had to include certain phenomena as free surface effects and coupling between fluid and a structure. Not to leave out easy reproducibility of the experiment in the tool, at no extra computational cost.

A sub-objective also set – to provide a comparison for an analytical solution developed concurrently as the experimental procedures were carried out.

6.1. CONCLUSIONS

- With motion enforcement being one of the key ingredients of this thesis in comparison to previous research, it can be concluded that the adopted motion system – rotary to linear motion mechanism showed significant improvement when compared in frequency and time domains with that from Rizos [1]. As such, this gives a good indication of reliable data to be used for validation.

- A comparison of the rigid body motion (RBM) data obtained during the experiments with the geometrical computation motion analysis reveals a significant difference in the amplitude of the peaks at integer multiples of the input oscillation frequency when compared with the amplitude of the base frequency. This difference can be ascribed to the *size* of the system being used; the geometrical computation system size (Amplitude = 1m, Connecting rod length = 5m) being much larger than the experimental system's size (Amplitude = 10mm, Connecting rod length = 0.5m). Reproducing one of the experimental parameters (Amplitude = 10mm, Frequency = 4Hz) in the geometrical computation, shows the amplitude of the peak at double of the input frequency is in the order of 0.005% of the input amplitude, as compared to a ratio of 5% obtained from the much larger system.

  This means that the size of amplitudes at integer multiples of the input frequency are dependent on the "size" of the system being used/analyzed. As such, this should be

noted when analyzing results obtained during any validation exercise of computational tools developed.

- The vibration data (displacements) obtained from polar locations on the membrane can provide validation data for comparison with data obtained by using *monitor points* in the computational domain when the experiment is reproduced therein.

- From the membrane vibration discrete measurements taken, it was noticed that the amplitude of the vibration at the centre was largest when compared to those at half-radius over a 180° span. This can be attributed to the bulging mode dominating the first natural frequency response of the membrane.

- Frequency dependence of membrane vibrations from one of the representative cases (Case Nr. 1) revealed an increase in response amplitude of the membrane with increasing frequency, up until 5.5 Hz. This frequency can be thought of as one of the natural frequencies (invariably the first natural frequency) of the coupled system. This, however, cannot be verified from experiments in other cases, as increasing the frequency with more than 50 ml of water in the plunger results in severe sloshing - which makes it rather impracticable to conduct measurements for other cases.

- Volume dependence, similar to frequency dependence, carried out keeping the oscillation amplitude and frequency constant, while varying the amount of water in the plunger showed an increasing volume of water in the plunger, there is an increasing amplitude of the membrane response at the input frequency. However, when the frequency in increased to 4.2 Hz, for an increasing volume of water, there is a decreasing amplitude.

- The current experiment in the pipeline involving a scanning vibrometer (see Appendix E) has the mirror system alignment as one of the crucial requirements. Asides this, the scanning vibrometer software is programmed in a way to not allow for the reference (input) signal subtraction from the output signal – which is actually needed to obtain the pure membrane deflections. This has to be taken into account in analyzing the data obtained from the scanning vibrometer software.

6.2. RECOMMENDATIONS FOR FUTURE RESEARCH

- The current methodology about obtaining complete membrane surface vibrations should be continued and completed, thereby obtaining possible mode shapes of the fluid-membrane coupled system.

- In analyzing the membrane vibration data obtained from the Polytec scanning vibrometer, data files have to be exported to be read by an external software (e.g MATLAB) in which the rigid body motion (reference signal) will be subtracted from each of the data points in the measurement mesh on the membrane. After this, the data can be imported back to the Polytec software where the mode shapes and frequency analysis would be done, or these can be done manually externally.

- The Modal Assurance Criterion (MAC) should be used to compare the mode shapes obtained from the surface vibration measurements (obtained from the Polytec Scanning

Vibrometer (PSV)) with those derived from analytical solutions developed by other research, as the MAC is frequently used for this [24]. The MAC would be suitable for this comparison because it is a statistical indicator that is only sensitive to large differences and not to small differences in mode shapes. This can cater for any errors of uncertainty in the conducted experiments and/or assumptions made for reduced-complexity in the analytical solutions developed. Thus, the MAC can serve as a validation means for the analytical solutions currently developed.

- An electrodynamical exciter (B&K type) together with a stinger, which can produce forced oscillations of very low amplitudes (order of tenths of millimeters) and high frequencies (order of kHz), should be used for the experiments involving the PSV measurement system. This would enable frequencies obtained in analytical solutions to be tested at, to obtain mode shapes which would be suitable for comparisons using the Modal Assurance Criterion suggested in the above point.

BIBLIOGRAPHY

[1] L. Rizos, *Reduced - complexity experiment for validating Fluid-Structure Interaction in ComFLOW*, Ph.D. thesis, Delft University of Technology (2016).

[2] P. GmbH, *Basic principle of vibrometry,* (2017).

[3] G. Group, *Vacuum sputter system for automative car mirror,* (2017).

[4] S. E. Hirdaris and C. Ge, *Introduction to Hydroelasticity of Ships,* Lloyd's Register Technical Association (2004).

[5] A. Bereznitski, *Practical Implications of Hydroelasticity in Ship Design loads Water / Air loads Water / Air,* **3**, 86 (2002).

[6] G. Hou, J. Wang, and A. Layton, *Numerical methods for fluid-structure interaction - A review,* Communications in Computational Physics **12**, 337 (2012).

[7] P. Gorf, N. Barltrop, B. Okan, T. Hodgson, and R. Rainey, *FPSO bow damage in steep waves,* Actes de colloques - ifremer , 37 (2002).

[8] G. Fekken, A. Veldman, and B. Buchner, *Simulation of Green Water Loading Using Navier-Stokes Equations* (1999).

[9] MARIN, *ComFLOW-3 Project Plan 3.0,* (2009).

[10] P. G. Bhuta and L. R. Koval, *Hydroelastic Solution of the Sloshing of a Liquid in a Cylindrical Tank,* Journal of the Acoustical Society of America **36**, 2071 (1964).

[11] P. G. Bhuta and L. R. Koval, *Coupled oscillations of a liquid with a free surface in a tank having a flexible bottom,* Zeitschrift füur angewandte Mathematik und Physik ZAMP **15**, 466 (1964).

[12] P. Tong, *Liquid motion in a circular cylindrical container with a flexible bottom.* AIAA Journal **5**, 1842 (1967).

[13] N. C. Small and T. Y. Tsui, *Hydroelastic oscillations of a liquid surface in an annular circular cylindrical tank with flexible bottom,* Journal of Spacecraft and Rockets **5**, 202 (1968).

[14] H. F. Bauer, S. Chang, and J. T. S. Wang, *Nonlinear liquid motion in a longitudinally excited container with elastic bottom,* AIAA Journal **9**, 2333 (1971).

[15] H. F. Bauer, *Hydroelastic vibrations in a rectangular container,* International Journal of Solids and Structures **17**, 639 (1981).

[16] H. F. Bauer, *Coupled frequencies of a liquid in a circular cylindrical container with elastic liquid surface cover,* Journal of Sound and Vibration **180**, 689 (1995).

[17] M. Chiba, *Nonlinear Hydroelastic Vibration of a Cylindrical Tank with an Elastic Bottom, Containing Liquid. Part II: Linear Axisymmetric Vibration Analysis,* Journal of Fluids and Structures **7**, 57 (1993).

[18] M. Chiba, *Axisymmetric free hydroelasric vibration of a flexural bottom plate in a cylindrical tank supported on an elastic foundation,* Journal of Sound and Vibration **169**, 387 (1994).

[19] M. Amabili, *Bulging Modes of Circular Bottom Plates in Rigid Cylindrical Containers Filled with a Liquid,* Shock and Vibration **4**, 51 (1997).

[20] M. Amabili and G. Dalpiaz, *Vibrations of base plates in annular cylindrical tanks: Theory and experiments,* Journal of Sound and Vibration **210**, 329 (1998).

[21] G. Berkovic and E. Shafir, *Optical methods for distance and displacement measurements,* Advances in Optics and Photonics **4**, 441 (2012).

[22] H. F. Bauer and M. Chiba, *Viscous Hydroelastic Vibrations in a Cylindrical Container With an Elastic Bottom,* Journal of Sound and Vibration **247**, 33 (2001).

[23] E. Optics, *Optical mirrors,* (2017).

[24] M. Pastor, M. Binda, and T. Harcarik, *Modal Assurance Criterion,* Procedia Engineering **48**, 543 (2012).

A

COMPUTATIONAL ROTARY TO LINEAR HARMONIC MOTION

To understand the translational motion of a point in a plane, converted from rotational motion, MATLAB was used for this computation. The configuration is as shown below. The crank radius is designated as the distance from the centre of the rotational motion, to a certain point; which corresponds to the amplitude of interest, of the translational harmonic motion. The connecting rod length is also specified – as the linear distance from the end of the crank radius to the point of application of the harmonic motion. This system of motion conversion is otherwise referred to as slider-crank mechanism. For the experimental setup of interest, this corresponds to the top of the plunger, to which a bearing and coupling are attached.

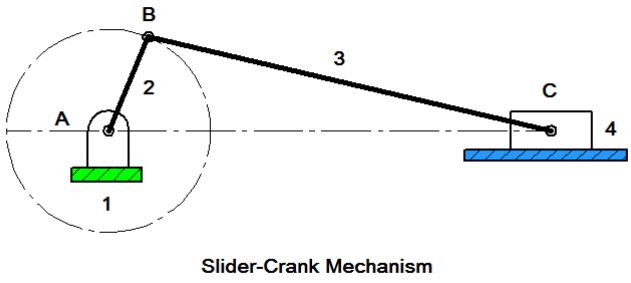

Figure A.1: Conversion of rotary to linear motion (crank-slider mechanism)

The kinematics of the motion the connecting rod end was studied, and a snippet of the MATLAB script used for this is given below. Upon computing and observing the plot of the displacement of the point of interest, it is seen that the displacement results in a sinus plot. Further, a curve fitting procedure is done with MATLAB, to obtain the computed displacement plot accurately, with the use of two or more perfect sinuses. This proves very useful, as it gives a basis upon which the signal from the triangulation laser displacement device can be compared; and, a good understanding of the motion signal that would be fed into the numerical solver during the validation process. In figure A.2 below, a plot of the displacement

of point C is shown. This is obtained from the MATLAB script beneath, being run for 3.2 seconds.

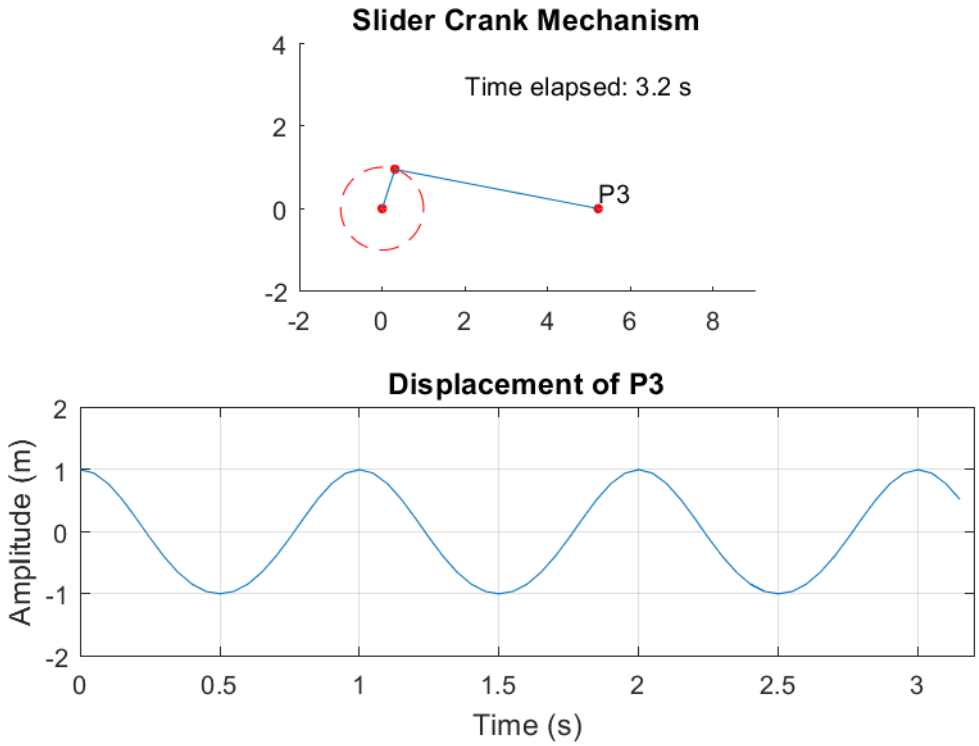

Figure A.2: Displacement plot of connecting rod end)

Upon careful analyses of the computational kinematics of the crank-slider motion signal, some trends are noticed upon Fast Fourier Transformation (FFT) of the displacement signal, which is shown in the figure A.3 below.

- There exists a peak at 2 Hz, which is expected, as that is the frequency input; but the amplitude of this peak does not correspond exactly with the input amplitude, 1 m, of the motion.
- A second peak exists at 4 Hz, which is double the input frequency and dominating peak. Although the amplitude of this peak is 0.04126 m, which when compared, is only about 4 % of the input amplitude.

Still considering the computational kinematics of the crank-slider motion, even more interesting trends are noted, when the signal is curve-fitted with sinuses. In the table below, the amplitudes of the signal resulting from sum of sines are shown, per number of fitted sine sums.

1-sine function: $f(x) = a_1 * sin(b_1 x + c_1)$
Coefficients (with 95% confidence bounds):
$a_1 = 1$ (0.9829, 1.017), $b_1 = 12.56$ (12.55, 12.57), $c_1 = 1.584$ (1.549, 1.619)

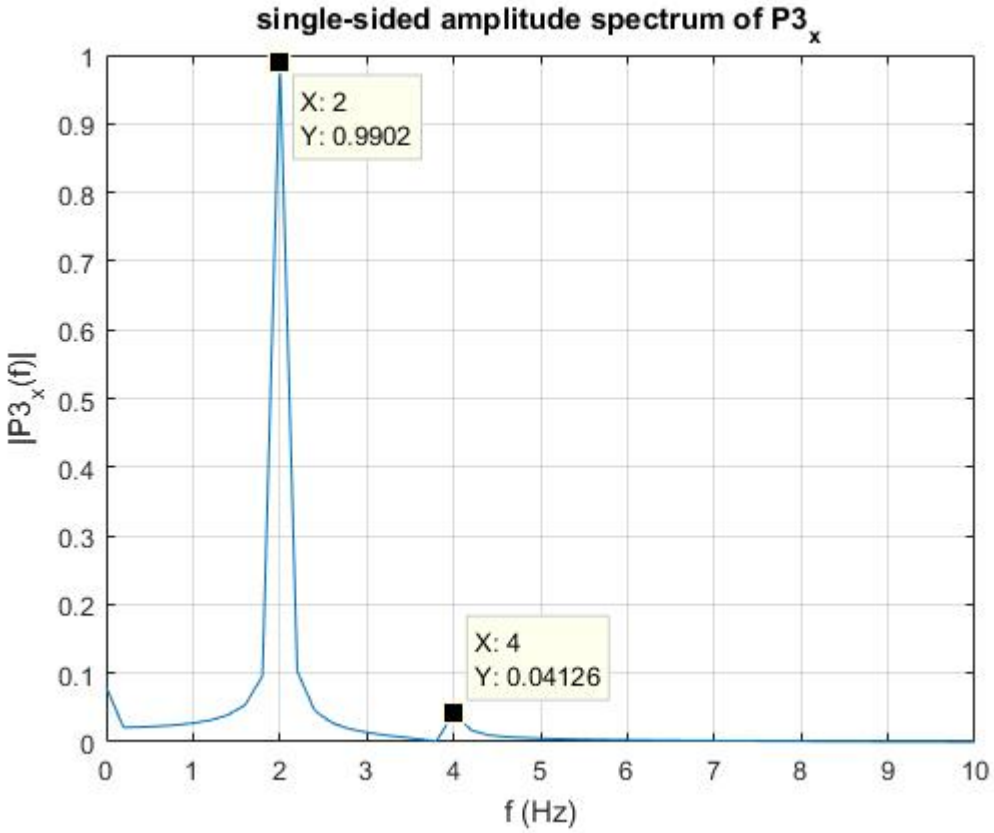

Figure A.3: FFT of crank-slider motion signal

Table A.1: Amplitudes per sine-fit

Sine-Fit	**Amplitude [m]**
1 sine	1.000
2 sines	1.003
3 sines	1.000

2-sine function: $f(x) = a_1 * sin(b_1 x + c_1) + a_2 * sin(b_2 x + c_2)$
Coefficients (with 95% confidence bounds):
$a_1 = 1.001\ (0.9907, 1.011)$, $b_1 = 12.56\ (12.56, 12.57)$, $c_1 = 1.575\ (1.554, 1.596)$
$a_2 = 0.05135\ (0.04033, 0.06237)$, $b_2 = 0.1716\ (-0.2685, 0.6116)$, $c_2 = -2\ (-3.244, -0.7557)$

3-sine function: $f(x) = a_1 * sin(b_1 x + c_1) + a_2 * sin(b_2 x + c_2) + a_3 * sin(b_3 x + c_3)$
Coefficients (with 95% confidence bounds):
$a1 = 1\ (1, 1)$, $b1 = 12.57\ (12.57, 12.57)$, $c1 = 1.571\ (1.571, 1.571)$
$a2 = 0.0504\ (0.05037, 0.05043)$, $b2 = 0.02292\ (0.01378, 0.03207)$, $c2 = -1.628\ (-1.654, -1.602)$
$a3 = 0.05051\ (0.05048, 0.05053)$, $b3 = 25.13\ (25.13, 25.13)$, $c3 = 1.571\ (1.57, 1.572)$

The above information indicates that fitting the signal with a sum of 3 sines gives a better approximation to the computed signal. This suggests that the output motion signal obtained by measuring the RBM motion during the experiments can be estimated with a fitted sum of 3

sines, and this can then be used as motion input during the numerical validation of ComFlow.

MATLAB SCRIPT

```
a = 1;              % crank radius
b = 5;              % connecting rod(slider) length
time = 5;           % time for simulation
t = 0:0.05:time;    % t is the time in seconds

w = 1*2*pi();       % Angular speed of the crank in rad/s
theta   = w*t;      % Angle between crank and horizontal line through crank centre

% Point P1          % Centre of crank rotation
P1 = [0;0];
alpha = asin(a*sin(theta)/b);
P2 = a*[cos(theta); sin(theta)];   % Point P2 % Connection point between crank and sli
P3 = [(a*cos(theta) + sqrt(b^2-a^2*(sin(theta)).^2)); (0*t)];    % Point P3 % End of s

P3_x = P3(1,:)-b;   % x-coordinate of P3
P3_y = P3(2,:);     % y-coordinate of P3

P3_Vx = diff(P3_x)./diff(t);    % x-component of P3 velocity
P3_Vy = diff(P3_y)./diff(t);    % y-component of P3 velocity

P3_V = sqrt(P3_Vx.^2 + P3_Vy.^2);   % Velocity of P3

for i = 1:length(t)     % loop to compute and plot the rotation

animation = subplot(2,1,1);
P2_traj = viscircles([0 0],a,'LineStyle', '--','LineWidth',0.5); %Point P2 trajectory
P1_circ = viscircles(P1',0.05);
P2_circ = viscircles(P2(:,i)',0.05);
P3_circ = viscircles(P3(:,i)',0.05);

crank   = line([P1(1) P2(1,i)], [P1(2) P2(2,i)]);       % Crank line
slider  = line([P2(1,i) P3(1,i)],[P2(2,i) P3(2,i)]);    % Slider line

axis(animation,'equal');
title('Slider Crank Mechanism')
set(gca,'XLim',[-a-1 b+4],'YLim',[-a-1 a+3]);

str1 = ['Time elapsed: ' num2str(t(i)) ' s'];   % Create string of time elapsed
P3_text = text(P3(1,i),P3(2)+0.4,'P3');         % Create string P3
Time = text(2,3,str1);

pause(0.005);       % interval to update the plot
```

```
    if i<length(t)      % Loop to delete the previous line/circles
        delete(crank);
        delete(P1_circ);
        delete(P2_circ);
        delete(slider);
        delete(P3_circ);
        delete(P3_text);
        delete(Time)

        disp_P3 = subplot(2,1,2);
        plot(disp_P3,t(1:i),P3_x(1:i));
        set(disp_P3,'XLim',[0 time],'YLim',[-2*a 2*a]);
        xlabel(disp_P3, 'Time (s)');
        ylabel(disp_P3, 'Amplitude (m)');
        title(disp_P3,'Displacement of P3');
        grid on;
    end

end

%% Curve fitting
fitting = fit(t',P3_x','sin3');

figure
plot(fitting)
hold on
plot(t,P3_x)
legend('fit','actual')
```

B

COMPUTING MEMBRANE TENSION - STATIC DEFLECTION APPROACH

As a precursor to estimating the coupled frequencies of the water-membrane system, the tension existing in the membrane due to a particular water height is to be known. A 2D schematic view of the plunger with the membrane at the bottom is as shown in Figure B.1 below. To solve for the tension in the clamped membrane at the bottom of the plunger due to a water height, an ordinary differential equation (Equation B.1) as formulated, is to be solved. A 2D simplification is used here, as the membrane and plunger have a circular cross-section, with the clamped boundary condition enforced uniformly around the membrane. So, with assumptions of material homogeneity and uniformly applied clamping on the membrane at the boundary, a 2D simplification is sufficient.

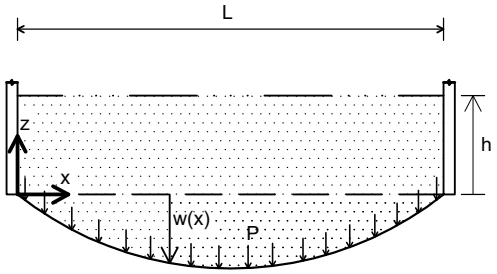

Figure B.1: 2D schematic of the static deflected membrane due to a water column

$$T\,\nabla^2 w + P = 0 \tag{B.1}$$

$$T\,\frac{\partial^2 w}{\partial x^2} + P = 0$$

Boundary Conditions:

$$w(0) = 0$$

$$w(L) = 0$$

where P = pressure due to the water height, acting on the membrane,
T = tension in the membrane, which is to be solved for, and
w = membrane deflection, which is a function of the spatial coordinate x.

The pressure, P, acting on the membrane is not uniform across the length of the membrane, but is a function of x and the deflection itself, w.

$$P = \rho g(h^* + w) \tag{B.2}$$

where h^* is the new water height after the membrane has been deflected, as illustrated in Figure B.2 below.

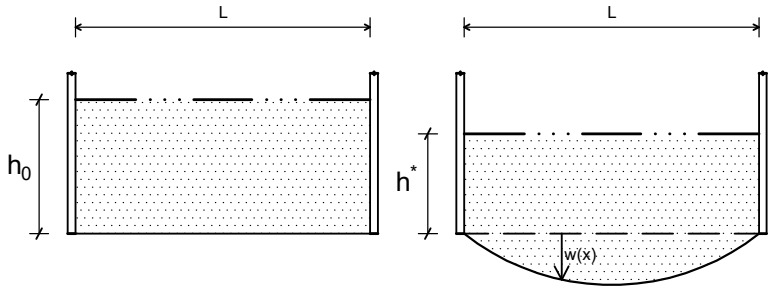

Figure B.2: 2D schematic of the water heights before and after deflection

And from the conservation of mass, assuming constant density

$$\int_0^L w(x)\mathrm{d}x + h^* L = h_0 L \tag{B.3}$$

Combining Equations B.1 and B.2 yields

$$\begin{aligned} \frac{\partial^2 w}{\partial x^2} &= -\frac{\rho g}{T}(h^* + w) \\ \frac{\partial^2 w}{\partial x^2} + \frac{\rho g}{T} w &= -\frac{\rho g h^*}{T} \end{aligned} \tag{B.4}$$

To solve the differential equation (Equation B.4), the homogeneous solution of the equation

$$\frac{\partial^2 w}{\partial x^2} + \frac{\rho g}{T} w = 0 \tag{B.5}$$

is sought in the form

$$w(x) = c_1 \cos(kx) + c_2 \sin(kx) \tag{B.6}$$

as it is assumed that the deflection of the membrane takes the shape of a sum of a sin and a cos function. From Equation B.6;

$$w' = -c_1 k \sin(kx) + c_2 k \cos(kx)$$
$$w'' = -c_1 k^2 \cos(kx) - c_2 k^2 \sin(kx)$$

Substituting the second spatial derivative into Equation B.5 result in the following cosine component:

$$-c_1 k^2 \cos(kx) + \frac{\rho g}{T} c_1 \cos(kx) = 0$$

From which,

$$k = \sqrt{\frac{\rho g}{T}} \tag{B.7}$$

To obtain the constants c_1 and c_2, the first boundary condition is applied to Equation B.6

$$\begin{aligned} w(0) &= 0 \\ 0 &= c_1 \cos(0) + c_2 \sin(0) \\ \implies c_1 &= 0 \\ \implies w &= A \sin(kx) \end{aligned}$$

Now substituting Equation B.6 into Equation B.4, to obtain the particular solution;

$$-k^2\Big(c_1 \cos(kx) + c_2 \sin(kx)\Big) + \frac{\rho g}{T}\Big(c_1 \cos(kx) + c_2 \sin(kx)\Big) = -\frac{\rho g h^*}{T} \tag{B.8}$$

Equation B.8 can be solved by using the variation of parameters approach, thus:

$$\begin{aligned} w &= c_1(t)\cos(kx) + c_2(t)\sin(kx) \\ w' &= -c_1(t)k\sin(kx) + c_2(t)k\cos(kx) + c_1'(t)\cos(kx) + c_2'(t)\sin(kx) \\ w'' &= -c_1(t)k^2\cos(kx) - c_2(t)k^2\sin(kx) - c_1'(t)k\sin(kx) + c_2'(t)k\cos(kx) \end{aligned} \tag{B.9}$$

As there is no variation of the constants with time, it can be assumed that

$$c_1'(t)\cos(kx) + c_2'(t)\sin(kx) = 0$$

From which

$$c_2'(t) = -c_1'(t)\frac{\cos(kx)}{\sin(kx)} \tag{B.10}$$

Substituting Equations B.9 and B.10 into Equation B.4;

$$\begin{aligned} -c_1'(t)k\sin(kx) + c_2'(t)k\cos(kx) &= -\frac{\rho g}{T}h^* \\ \implies -c_1'(t)k\sin(kx) - c_1'(t)k\cos(kx)\frac{\cos(kx)}{\sin(kx)} &= -\frac{\rho g}{T}h^* \\ \implies -c_1'(t)k\sin^2(kx) - c_1'(t)k\cos^2(kx) &= -\frac{\rho g}{T}h^*\sin(kx) \\ \implies c_1'(t) &= \frac{\rho g h^*}{kT}\sin(kx) \end{aligned}$$

Thus,

$$c_2'(t) = -\frac{\rho g h^*}{kT}\cos(kx)$$

Integrating $c_1'(t)$ and $c_2'(t)$

$$\begin{aligned} \implies c_1 &= -\frac{\rho g h^*}{kT}\cos(kx) + \alpha_1 \\ \text{and} \qquad c_2 &= -\frac{\rho g h^*}{kT}\sin(kx) + \alpha_2 \end{aligned}$$

Substituting the values of c_1 and c_2 into Equation B.6;

$$\begin{aligned} w &= -\frac{\rho g h^*}{kT}\cos^2(kx) - \frac{\rho g h^*}{kT}\sin^2(kx) + \alpha_1\cos(kx) + \alpha_2\sin(kx) \\ \implies w &= -\frac{\rho g h^*}{kT} + \alpha_1\cos(kx) + \alpha_2\sin(kx) \end{aligned}$$

Now applying both the first and the second boundary conditions;

$$\begin{aligned} w(0) = 0 \qquad &\implies 0 = -\frac{\rho g h^*}{kT} + \alpha_1 \\ w(L) = 0 \qquad &\implies 0 = -\frac{\rho g h^*}{kT} + \alpha_1\cos(kL) + \alpha_2\sin(kL) \end{aligned}$$

This gives

$$\begin{aligned} \alpha_1 &= \frac{\rho g h^*}{kT} \\ \text{and} \qquad \alpha_2 &= \frac{1-\cos(kL)}{\sin(kL)}\frac{\rho g h^*}{kT} \end{aligned}$$

$$\text{Hence,} \qquad w = \frac{\rho g h^*}{kT} + \frac{\rho g h^*}{kT}\cos(kx) + \left(\frac{1-\cos(kL)}{\sin(kL)}\right)\sin(kx) \tag{B.11}$$

Equation B.11 together with Equation B.3 (reproduced here below)

$$h^* L + \int_0^L w(x)\mathrm{d}x = h_0 L$$

can be used to compute the tension, **T** from a measurement of w_{max}; i.e. the maximum deflection at $x = L/2$, due to a water column.

C

First Experiment Schematic

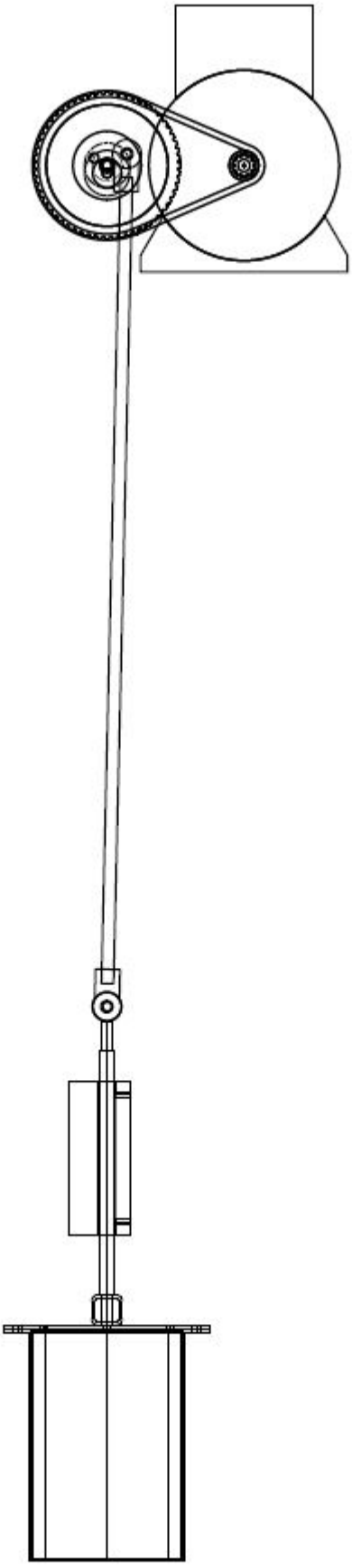

Figure C.1: Conversion of rotary to linear motion (crank-slider mechanism)

D

Motion signal deviation from Sine fit (Expanded view)

In order to make an estimate of the deviation of the motion signal from the sum of 3− sines with which a fit was done, a plot with horizontal grid lines at 0.1 mm steps is used. Figure D.1 below shows the case with oscillation amplitude of 10 mm and frequency of 2 Hz. This plot also gives an indication into which of the 3 load cases gives better rigid body motion signal.

In the three load cases, there exists an underlying dominant signal of 0.2 mm amplitude. However, with increasing loads, the sine-fit deviations are seen to be have lesser amplitudes. Hence, it can be concluded that the motion system behaves better with more load in the system.

Figures D.2 and D.3 show the deviation of the motion signal from the sine fit, for oscillation amplitudes of 5 mm and 15 mm respectively. both with frequency of 2 Hz. As seen, they follow the same trend that the motion signal fits better with the sine-fit, for increasing load in the system.

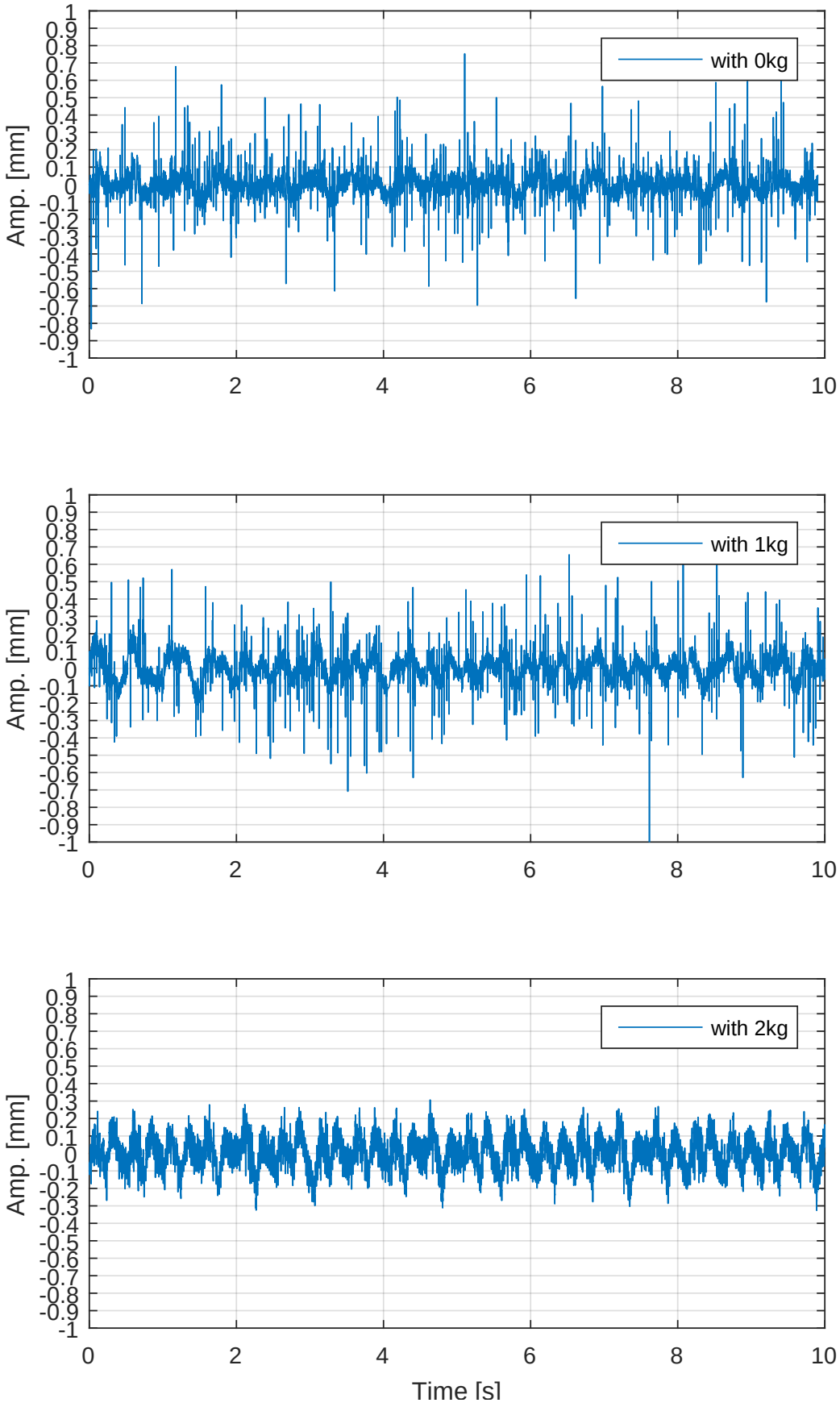

Figure D.1: Deviation of motion signal from since-fit for varying loads in the system. A10mm f2Hz

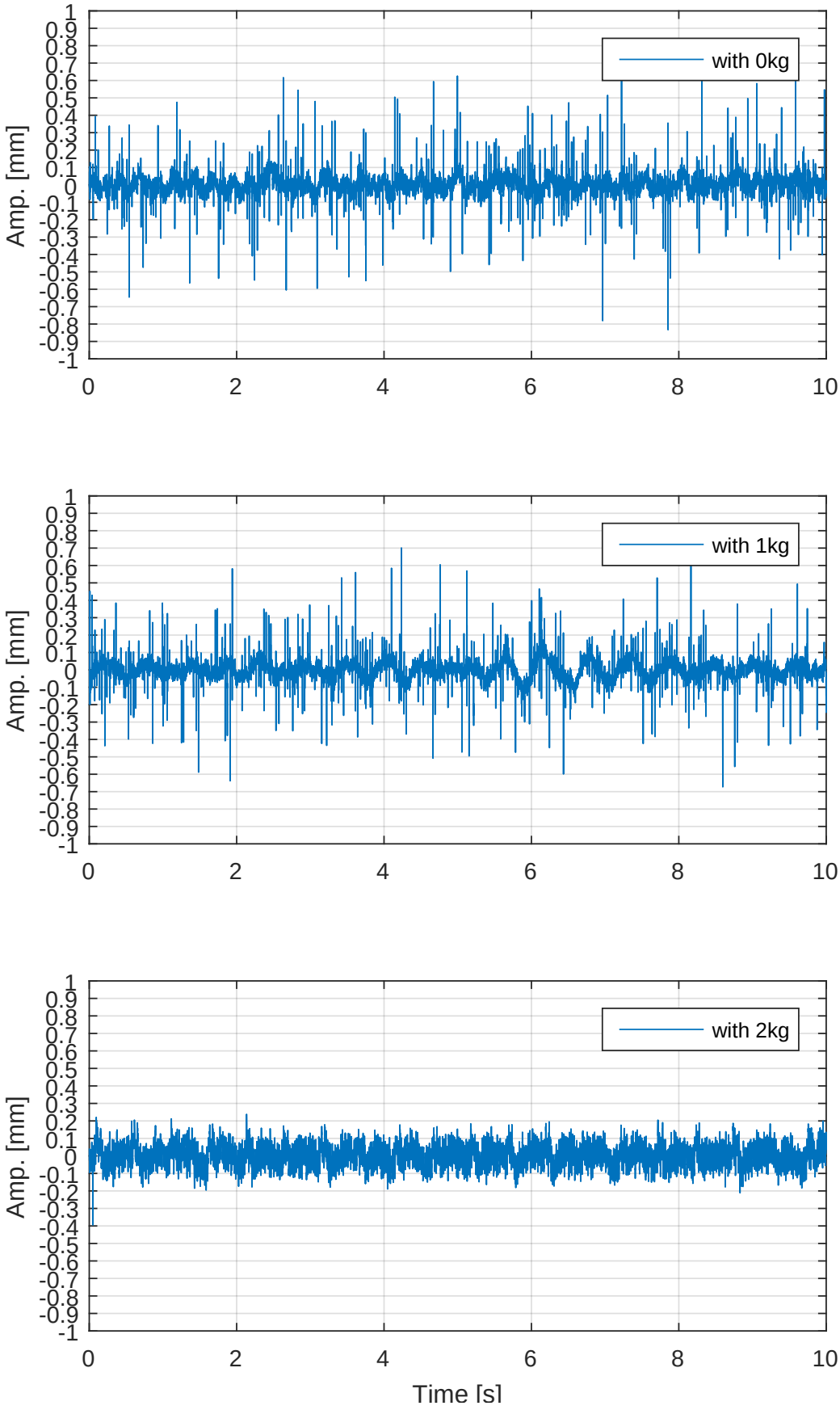

Figure D.2: Deviation of motion signal from since-fit for varying loads in the system. A5mm f2Hz

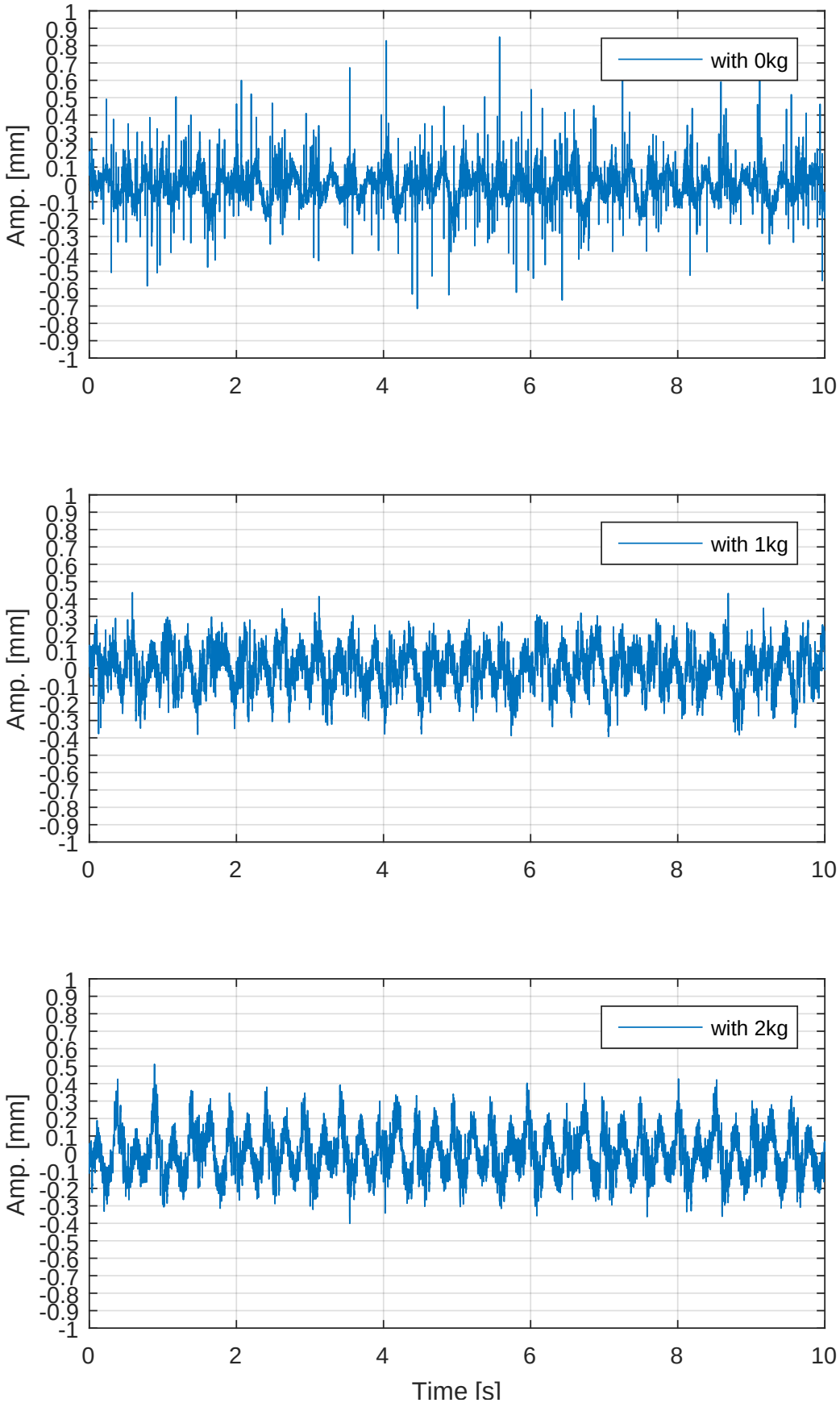

Figure D.3: Deviation of motion signal from since-fit for varying loads in the system. A15mm f2Hz

E

MEMBRANE SURFACE VIBRATION MEASUREMENTS

E.1. INTRODUCTION/MOTIVATION

After conducting experiments involving the use of a laser triangulation measurement device, no particular trend was noticed - either due to frequency, water volume or polar location variation. This can be partly attributed to the measurement technique which involved taking measurements of discrete points on the membrane. As a result of the inherent limitation of the initial technique used, it is sought to take measurements of the entire membrane surface during oscillation of the water-plunger-membrane system. This measurement can only be achieved by using a scanning measurement device - a device that measured multiple locations on the surface of a vibrating surface concurrently. The Polytec Scanning Vibrometer (PSV) comes in handy. The PSV is basically a scanning Laser Doppler Vibrometer (LDV) which has the capability to measure multiple points, as defined by a grid, on a vibrating structure.

Another motivation for this further experiment is that the PSV only requires one setup for all measurement points, as compared to adjusting measurement locations when using a single-point measurement device, as in Section 2.5.1. This is advantageous as it eliminates any tendencies for errors during the experiment.

E.2. MEASUREMENT SYSTEM: PSV-400

The PSV consists of a compact sensor head, a workstation and the software which works to control the scanners, coordinate data processing and provide data visualization. The sensor head is made up of a laser interferometer, scanning unit and a video camera. The workstation consists of the vibrometer controller, data acquisition and data management system. The main component in the PSV head is the laser Doppler vibrometer – a very precise optical transducer used for determining the vibration velocity and displacement at a point by sensing the frequency shift of back scattered light from a moving surface.

During experiments, a grid will be defined on the surface of interest – the membrane. The laser beam will automatically scan the whole grid defined by moving to each point and make a vibration measurement of each of the predefined points. While doing this, the measurement systems works to ensure the laser is optimally focused during measurements, through

a validation process. This is possible by monitoring and optimizing the signal-to-noise ratio. Upon completion of the scan, appropriate frequencies can be chosen and then the deflection shape in convenient presentation modes can be displayed and animated. These provide a very useful means of studying the membrane behaviour.

During the scanning, frequency spectra and time traces are displayed for the vibrometer and any external reference signal. The vibrometer data can be in terms of displacement, velocity or acceleration. In addition, a Frequency Response Function (FRF) can be displayed.

E.2.1. MEASURING PRINCIPLE

The PSV-400 utilizes the Doppler-effect technology for determining vibration displacement and velocity at a fixed point, by sensing the shift in frequency of back-scattered light (wave) from the surface of interest. The measured frequency shift of the reflected wave from the moving object is a function of the wavelength of the emitted wave and the object's velocity – which is itself determined by using the high-precision laser interferometer housed in the LDV, which works on the principle of optical interference, depicted in Figure E.1 below.

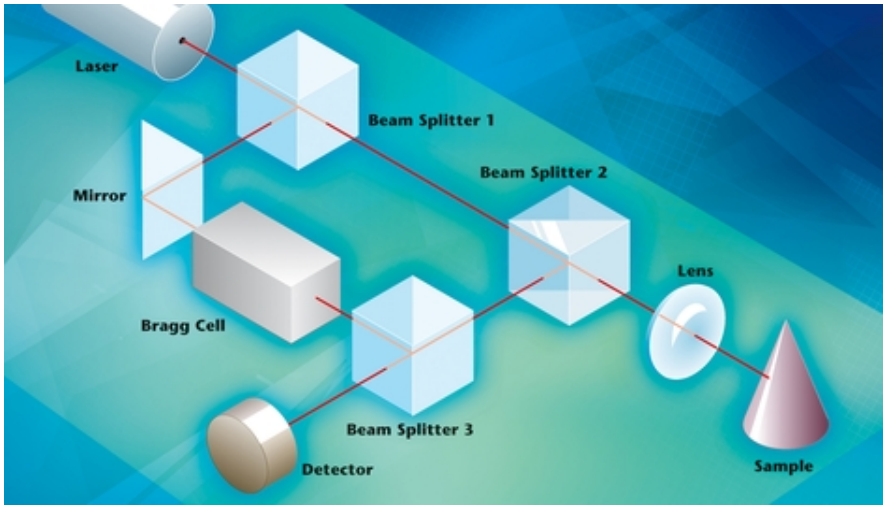

Figure E.1: Optical interference working principle of the LDV [2]

The laser interferometer's working principle uses the overlapping of two coherent beams of light, with intensities I_1 and I_2, resulting in an intensity defined by

$$I_{tot} = I_1 + I_2 + 2\sqrt{I_1 I_2 \cos\left(\frac{2\pi(r_1 - r_2)}{\lambda}\right)}$$

in which the last term, called the *interference* term, relates to the difference in path lengths of the two light beams. As in Figure E.1, when the laser beam (Helium-Neon) is emitted, it is split by the first beam-splitter (BS 1) into a measurement beam and a reference beam. The measurement beam passes through a second beam-splitter (remaining undeflected) (BS 2) before it is sent through a lens to the object under investigation. The object reflects the beam, which is deflected by BS 2 to be merged with the reference beam by a third beam-splitter (BS 3), before being directed onto the detector. Since the path length is relatively constant over time, any motion in the investigated object would generate a fringe (dark and bright) pattern on the detector.

A change in the length of the optical path per unit time shows itself as the Doppler frequency shift on the measurement beam. This implies that the modulation frequency of the fringe pattern is directly proportional to the velocity of the test object. Due to the independence of the fringe pattern (and frequency shift) of the test object motion (motion toward and away from the interferometer), a Bragg cell is useful in the LDV head. The Bragg cell is an acousto-optic modulator which is located in the line of action of the reference beam, which works to shift the light frequency by 40 MHz. This generates a modulation frequency of the fringe pattern of 40 MHz when the object is at rest. If the test object then moves towards the interferometer, this modulation frequency is reduced and if it moves away from the vibrometer, the detector receives a frequency higher than 40 MHz. This now enables the detection of the direction of the test object movement as well as its amplitude.

As opposed to normal measurement devices, the LDV does not transform the measured velocity and/or displacement of the test object to a voltage proportional to velocity (or displacement). Instead, the LDV makes a count of the fringes (bright-dark pattern) on the detector. Interpolation techniques in the LDV can be used to obtain very good resolutions ~ 2 nm.

E.3. METHODOLOGY

The PSV's measurement operation is in such a way that the test object has to be in a plane perpendicular to the laser beam. The tripod stand on which the scanning head sits restricts the angular orientation of the head, in such a way that the scanning head cannot be made to point vertically upwards - which would be ideal for this experiment. However, the partially-filled plunger as used in the previous experimental setup is only able to oscillate in a vertical direction. This poses a practical issue in orienting the measurement device to obtain needed experimental data.

To overcome this practical issue, a technique is developed in which a mirror would be placed underneath the plunger, at a 45° angle to the horizontal. This would take the laser beam incident from the PSV scanning head, diverting it by exactly 90° and reorienting it to be incident on the membrane on the plunger's bottom. This technique is thus sensitive to the angular orientation of the mirror, as any slight variation in the intended 45° angle would result in the laser beam misdirected on the membrane surface.

E.3.1. SETUP

1. **Front-coated Mirror**

   As stated in the previous paragraph, a mirror is needed for the experiment to be feasible. As in optics, there are broadly two categories of mirror; viz back-coated mirrors and front-coated mirrors. Based on the principle of operation of both types of mirrors (Figure E.2), the mirror to be used in this experiment is a front-coated mirror. The reasoning behind this is that a ray of light entering a back-coated mirror would first have some part of it reflected as the ray passed from the air into the mirror material (glass). Only a percentage of the incident ray would go on to the reflective material of the mirror, to be reflected. This results in a loss of integrity of the incident ray – which cannot be tolerated when using the PSV. Contrary to a back-coated mirror, the front-coated mirror has the reflective material at the *front* of the mirror, and with a high-quality mirror, a reflectance of ~ 85% of the incident rays hitting the mirror are assured.

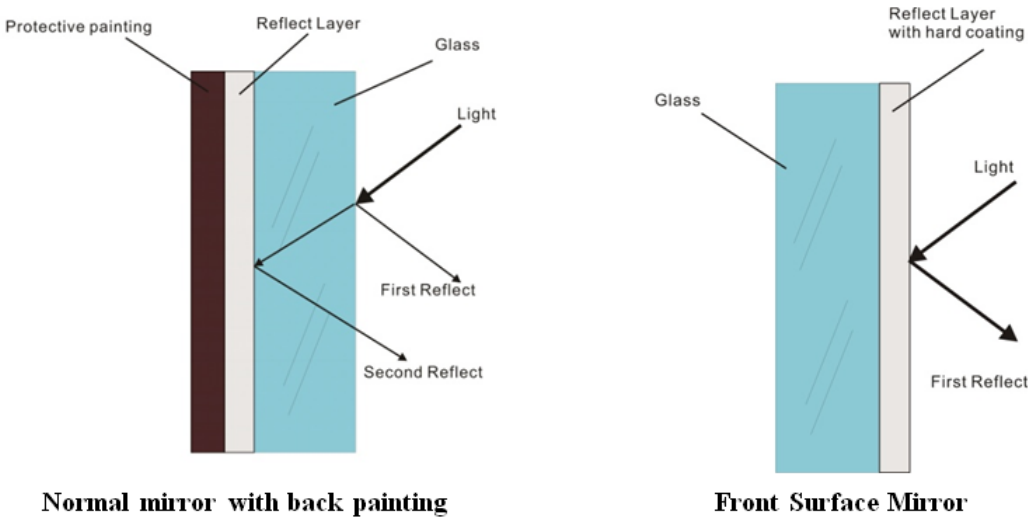

Figure E.2: Illustration of front-coated and back-coated mirrors [3]

With the type of mirror to be used already determined, it should also be noted that the mirror is to be of a high quality with respect to the surface flatness and quality. Surface flatness, being specified as a fraction (or multiple) of the wavelength (λ) of the incident beam, can range from one-twentieth of the wavelength to six times the wavelength [23], with the former flatness value being of a higher quality than the latter.

2. **Mirror mount**

   With the mirror type and characteristics defined, a method for supporting the mirror on the setup has to be developed. One way to mount the mirror would be to fix it on the main support structure of the experimental setup, but this would induce vibrations in the mirror due to motions of the mechanical drive system. Vibrations in the mirror would compromise the integrity of the LDV beam's deflection. To overcome this limitation, a *Manfrotto 055PROB*™ tripod is used, fitted with a *Manfrotto 410 Junior Geared Head*™ which allows for all 3 angular degrees of freedom (DOF) – about the x-, y- and z- axes (Figure E.3).

   The mirror support head has angular scales on each of the 3 axes of rotation for adjusting the orientation of the mirror; 45° to the horizontal as intended.

3. **Mirror size and location**

   As it has been explained that the mirror to be used in the experiment is to be of a high quality, one influencing factor stemming from this is the cost of the mirror. As such, it is desired that the mirror be as small as practically possible for the intended use. The mirror size, however, also depends on the distance from the membrane at the plunger bottom, as the mirror must be able to reflect the total surface of the membrane, in order for the PSV to scan it properly.

   A quick market survey of such intended mirrors reveals that they come in sizes of inches corresponding to their diameters, with 1 inch being the smallest size. As a result of this, an analysis is made, with respect to the mirror location and the closest location of

(a) Head with x-, y- and z- axes rotations

(b) Tripod for mirror support

Figure E.3: Manfrotto 055PROB™ tripod with Manfrotto 410 junior geared head™ for mirror support

the scanning head to the mirror, to achieve a full field of view of the plunger bottom. Here, the total distance of travel of the laser ray from the membrane is important, as the scanning head has a minimum stand-off distance (See Table E.1). After clarifying the factors affecting the mirror to be used, and with the diameter (size) of the mirror being the parameter to be optimized here, a few cases of the setup are investigated and represented in the schematic in Figure E.4 below.

PSV 400 Sensor Head Specifications

Laser type	Helium-Neon laser
Laser class	Class 2
Laser wavelength	633 nm
Working distance	40 mm – 100 m (MR Lens)
Working distance	35 mm – 100 m (LR Lens)
Sample size	few mm^2 up to several m^2
Scanning range	±20°
Angular resolution	< 0.002°
Scan speed	Up to 30 points/s (typical)

Table E.1: PSV 400 sensor head technical data

From figure E.4, a mirror size of 1 inch (= 25.4 mm) shows that the scanning head would be about only 20 cm from the mirror, and encroaching into the support structure. This is not desirable because of the tendency of water spilling out of the plunger during motion, which could severely damage the PSV. A 2 inch mirror allows for the scanning head to be a minimum distance of about half a meter from the support structure. A 3 inch mirror allows for even a further distance of the scanning head from the support structure, which is ideally safer. But due to the cost constraint, the 2 inch mirror function

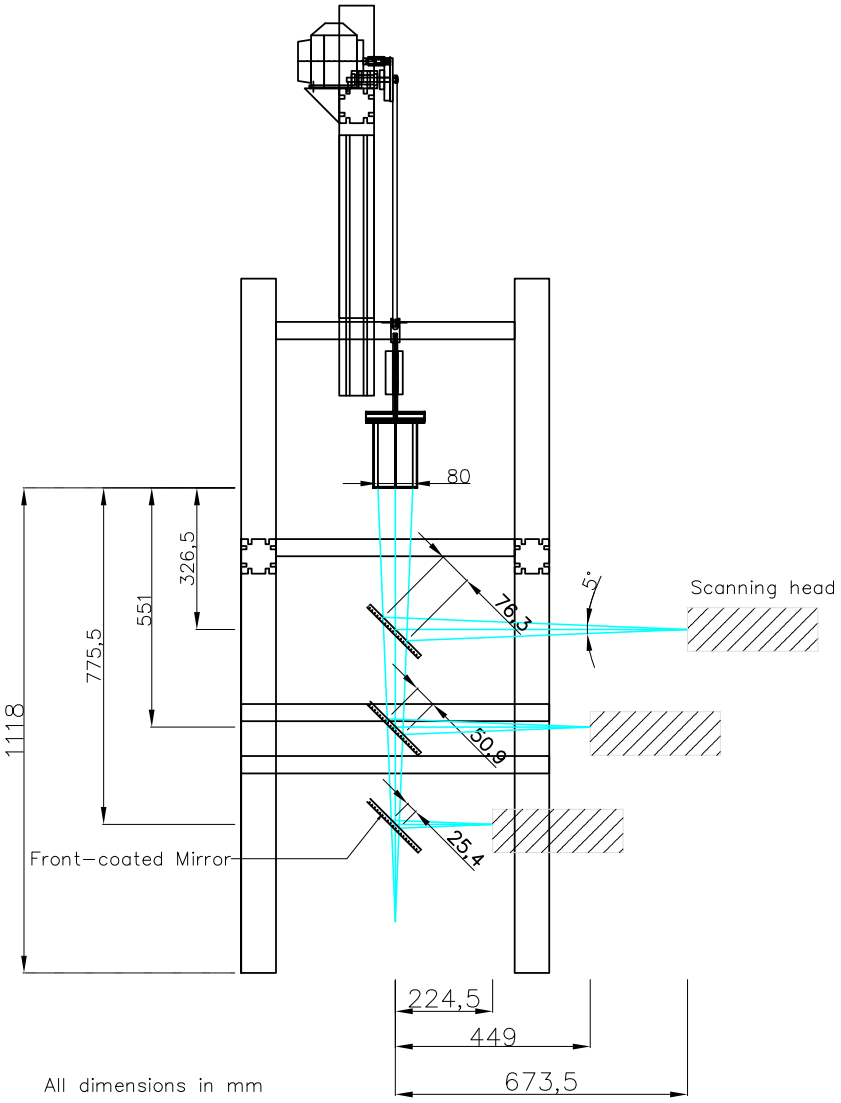

Figure E.4: Side-view of experimental setup with three hypothetical mirror/scanning head locations

optimally for the intended experiments. It should however be noted that in all the three mirror cases, the total working distance exceeds the minimum of 40 mm as specified by the manufacturer (Table E.1)